

1 *Revision 3* Word count: 6897

2 **Reconstructing volatile exsolution in a porphyry ore-**
3 **forming magma chamber: Perspectives from apatite**
4 **inclusions**

5 **Wenting Huang^{1, 2, 3}, Michael J. Stock², Paul C. Guyett^{2, 4}, Xiao-Ping Xia^{1, 3*},**
6 **Huaying Liang^{1, 3*}, Weidong Sun⁵, and Chun-kit Lai⁶**

7 *¹ Guangzhou Institute of Geochemistry, Chinese Academy of Sciences, Guangzhou*
8 *510640, China*

9 *² Department of Geology, Trinity College Dublin, Dublin, Ireland*

10 *³ CAS Center for Excellence in Deep Earth Science, Guangzhou, 510640, China*

11 *⁴ iCRAG, SFI Research Centre for Applied Geosciences, Ireland*

12 *⁵ Center of Deep Sea Research, Institute of Oceanology, Chinese Academy of*
13 *Sciences, Qingdao 266071, China.*

14 *⁶ Global Project Generation and Targeting, Fortescue Metals Group Ltd., East Perth*
15 *WA 6004, Australia*

16 **Abstract**

17 Porphyry-type deposits in the shallow crust (3-5 km) are formed from metal-rich
18 fluids exsolved from underlying magma chambers (5-15 km). However, a direct
19 volatile record of the fluid exsolution in the magma chamber is commonly lacking.
20 Here, we analyse the compositions of apatite inclusions (in biotite and plagioclase
21 phenocrysts, and fully-/partly-included in zircon microphenocrysts) and the apatite in
22 groundmass from the largest Cretaceous Luoboling porphyry Cu–Mo deposit in South
23 China. In combination with thermodynamic models, we reconstructed the volatile

24 behaviour in the ore-forming magma. The analysed apatites are magmatic in origin,
25 without hydrothermal overprint, as indicated by their homogeneous
26 cathodoluminescence (CL) and higher Cl and REE contents than typical hydrothermal
27 apatite. Apatite inclusions fully enclosed in zircon show decreasing X_{Cl}^{Ap}/X_{OH}^{Ap} (1.5-
28 0.1) with increasing X_F^{Ap}/X_{OH}^{Ap} (0.4-3.3) and X_F^{Ap}/X_{Cl}^{Ap} (0.5-21), and display a steep
29 drop in X_{Cl}^{Ap} at approximately constant X_{OH}^{Ap} in the ternary F–Cl–OH plot. These trends
30 follow the modelled compositional trajectories of isobaric H₂O-saturated
31 crystallisation, indicating volatile exsolution during or before zircon crystallisation in
32 the magma chamber. Groundmass apatite crystals, phenocryst-hosted apatite
33 inclusions and apatite inclusions, which are partially enclosed by zircon
34 microphenocrysts, have comparable volatile compositions, with much higher
35 X_F^{Ap}/X_{OH}^{Ap} (1.7-78.8) and X_F^{Ap}/X_{Cl}^{Ap} (2.3-37.5) but lower X_{OH}^{Ap} and X_{Cl}^{Ap} than those fully
36 enclosed in zircon. Compositional similarities between these crystals in different
37 textural associations indicate that the phenocryst-hosted apatite inclusions do not
38 preserve their original volatile records at the time of entrapment, and the volatile
39 compositions were overprinted by later re-equilibration with the residual melt and the
40 exsolved magmatic fluids. Given the porphyry magma is highly oxidized, and the
41 sulfides phases would be unstable in such circumstance, we suggest that volatile
42 exsolution in the magma chamber is essential for the Cl and Cu-Mo extraction from
43 the melts and therefore the porphyry mineralization. In this study, only zircon-hosted
44 apatite inclusions appear to best record the magmatic volatile compositions in a
45 porphyry system faithfully. Therefore, using apatite hosted in other minerals or
46 groundmass compositions to unravel magma volatile contents in porphyry Cu system
47 should be conducted with caution.

48 **Keywords:** porphyry deposit, apatite inclusions, volatile exsolution, diffusional re-
49 equilibration

50 **1. Introduction**

51 Porphyry-type deposits contribute >75% and 25% of the global Cu and Au
52 reserves, respectively (Sillitoe, 2010). They are usually associated with small shallow-
53 emplaced (1-5 km) intermediate–felsic porphyries, mineralised by the fluids exsolved
54 from underlying magma chambers (5-15 km) (Chiaradia, 2021; Hedenquist and
55 Lowenstern, 1994; Richards, 2011; Sillitoe, 2010). Since Cu, Mo, Au, Cl, and S are
56 strongly partitioned into buoyant magmatic fluids (Audetat and Simon, 2012;
57 Lowenstern, 1994; Williams-Jones and Migdisov, 2014), the volatile exsolution in the
58 magma chamber was suggested to play an essential role in metal extraction and
59 mineralisation (Candela and Holland, 1986; Cooke et al., 2005; Halter et al., 2002;
60 Huber et al., 2012; Nadeau et al., 2010). However, a direct continuous volatile record
61 of the fluid exsolution in the magma chamber is still lacking, as the melt inclusions,
62 the conventional medium for tracing magmatic volatiles, is often compromised by
63 post-entrapment crystallisation and volatile diffusion in the plutonic (porphyry)
64 systems (Bucholz et al., 2013; Gaetani et al., 2012).

65 Apatite [Ca₅(PO₄)₃(F, Cl, OH)] incorporates F⁻, Cl⁻, and OH⁻ directly into its
66 crystal structure within a dedicated volatile site (Z). Apatite volatile analysis has
67 recently received increasing attention as a new effective way to constrain the
68 magmatic volatile concentration and behaviour in terrestrial (e.g., Boyce and Hervig,
69 2008; Humphreys et al., 2021; Stock et al., 2018) and extraterrestrial (e.g., Boyce et
70 al., 2014; McCubbin and Jones, 2015) systems. Apatite inclusions in volcanic rocks
71 can preserve the record of volatiles at the time of entrapment, even where melt
72 inclusion H₂O concentrations have been modified by post-entrapment processes

73 (Stock et al., 2018; Stock et al., 2016). Notably, zircon-hosted apatite inclusions have
74 been proven resistant to re-equilibration and hydrothermal alteration in granitic and
75 porphyry systems (Bell et al., 2018; Bell et al., 2015; Kendall-Langley et al., 2021; Li
76 et al., 2021; Meng et al., 2022). Thus, apatite inclusions in minerals can potentially
77 record the volatile evolution in porphyry ore-forming magmas.

78 The Luoboling Cu–Mo porphyry deposit was selected for study. The deposit is
79 genetically associated with the largest Zijinshan epithermal-porphyry Cu-Au-Mo ore
80 field in Asia (Fig. 1, Huang et al., 2018; Jiang et al., 2013). We present analysis of the
81 volatile compositions of unaltered apatite inclusions in plagioclase and biotite
82 phenocrysts, in the groundmass, and the tiny apatite inclusions in zircon
83 microphenocrysts from the syn-mineralisation granodiorite porphyry. The apatite
84 inclusions with various textures (phenocryst-, groundmass-hosted, fully included by
85 zircon/partly included by zircon) place constraints on the time when apatite inclusions
86 were isolated from their host melt and may reflect the volatile compositions across the
87 porphyry ore-forming magma evolution. Compared with the apatite thermodynamic
88 model of Stock *et al.* (2018), we unravelled the behaviour of volatile species and
89 delineated a continuous volatile evolution trend for the causative magma of the
90 Luoboling porphyry deposit. This provides insights into the behaviours of both
91 volatile components (Cl and H₂O) and ore metals (Cu and Mo) they carried.

92 **2. Geological Background and Ore Geology**

93 The Zijinshan in southeastern China (Fig. 1a) is the largest epithermal-porphyry
94 orefield in Asia, which contains many epithermal and porphyry deposits associated
95 with the Cretaceous Paleo-Pacific subduction (Fig. 1b) (Huang et al., 2018; Jiang et
96 al., 2013; So et al., 1998; Zhong et al., 2014). These deposits contain 399 metric
97 tonnes (t) Au, 6400 kt Ag, 4.137 Mt Cu, and 110 kt Mo (Zhang, 2013; Zhong et al.,

98 2014). In particular, the Luoboling porphyry Cu–Mo deposit in northeastern Zijinshan
99 contains 1.4 Mt Cu @ 0.3% and 110 kt Mo @ 0.036% (Zhong et al., 2014).

100 The Neoproterozoic Louziba Group is the oldest stratum in the Zijinshan ore
101 field, which comprises meta-clastic rocks (Fig. 1b). These rocks are unconformably
102 overlain by Upper Devonian and Carboniferous sedimentary rocks. The Lower
103 Cretaceous Shimaoshan Group volcanic rocks are exposed across the Zijinshan
104 orefield (Fig. 1b), which yielded zircon U–Pb ages of 113–93 Ma (Jiang et al., 2013).

105 Intrusions in the Zijinshan ore field were emplaced in the Mesozoic, including
106 the Zijinshan granite complex (zircon U–Pb age: 154–165 Ma; Li et al., 2015), Caixi
107 monzogranite (zircon U–Pb age: 157–150 Ma; Jiang et al., 2013), Sifang granodiorite
108 (zircon U–Pb age: 112 ± 1 Ma; Jiang *et al.*, 2013), Luoboling granodiorite porphyry
109 (zircon U–Pb age: 97–103 Ma; Huang et al., 2013), and the Zhongliao porphyritic
110 granodiorite (zircon U–Pb ages of 95.9 ± 0.6 Ma; Li and Jiang, 2014). The Luoboling
111 granodiorite porphyry intrudes the Sifang granodiorite and Caixi monzogranite (Fig.
112 1b). The Zhongliao porphyritic granodiorite was revealed by drilling to underly the
113 Luoboling granodiorite porphyry (Fig. 2).

114 Porphyry mineralisation occurred mainly in the Luoboling granodiorite
115 porphyry. There are three main hydrothermal alteration stages (I to III) at Luoboling:
116 (I) potassic–silicic (K–Q) alteration; (II) phyllic (Phy) alteration; and (III) alunite–
117 dickite (Alu–Di) alteration, which are spatially associated with pyrite, bornite, and
118 digenite mineralization (So et al., 1998, Zhong et al., 2014). This alteration is
119 generally located in the exocontact of the Zhongliao porphyritic granodiorite (Fig. 2).
120 The porphyry Cu–Mo mineralisation generally occurred (as veinlet or disseminated
121 sulfides) where the K–Q alteration was overprinted by Phy alteration (K–Q+Phy). Ore

122 minerals at the Luoboling deposit include mainly pyrite, chalcopyrite, and
123 molybdenite.

124 **3. Sample Description**

125 Luoboling granodiorite porphyry samples (LBL-82 and LBL-77) were collected
126 from drill holes ZK405 at 680 m and 682 m depth, respectively. The granodiorite
127 porphyry includes phenocrysts (>0.5 mm) of plagioclase (~25 vol.%), biotite (~5
128 vol.%), and quartz (~5 vol.%) within a groundmass of quartz (~25 vol.%), K-feldspar
129 (~25 vol.%), biotite (~10 vol.%), plagioclase (~5 vol.%), and anhydrite (<5 vol.%)
130 (Fig. 3a). Accessory minerals (<5 vol.%) mainly consist of apatite, zircon, and
131 magnetite. The samples are weakly altered, yet most minerals appear fresh (Fig. 3a).

132 Zircon occurs in the groundmass (Fig. 3b) or as inclusions within other
133 phenocryst phases (Fig. 3c). Zircons in the groundmass are more elongate than those
134 hosted in the phenocrysts, and their length-width ratios are >3 for the former (Fig. 3b)
135 and 2-3 for the latter (Fig. 3c). Tiny apatite inclusions widely occur within the zircon
136 grains (Fig. 4). Apatite crystals occur mainly as inclusions within plagioclase (Fig. 3c)
137 and biotite phenocrysts (Fig. 3d) or in the groundmass (Fig. 3e-f). The groundmass-
138 hosted apatites are either enclosed by other phases (i.e., quartz and K-feldspar) or as
139 interstitials among other minerals (Fig. 3e). Most apatite crystals are euhedral and
140 clear without fluid or mineral inclusions (Fig. 3c-e). Some apatite grains, especially
141 the apatite micro-phenocrysts (> 200 μm) in the groundmass, were altered and contain
142 abundant fluid inclusions and monazite inclusions (Fig. 3f).

143 In this study, we divided the primary apatite inclusions into three types based on
144 their occurrences, namely those (1) included in zircon; (2) included in phenocrysts;
145 (3) in the groundmass.

146 **4. Sample Preparation and Methods**

147 **4.1 Sample preparation**

148 Polished thin sections were made from each sample. About 1 kg of the
149 granodiorite porphyry was crushed and sieved to extract zircon microphenocrysts
150 from the 300–350 μm size fraction using conventional density and magnetic
151 separation techniques. Euhedral, clear zircon crystals ($> 200\mu\text{m}$) were handpicked
152 under a binocular microscope, which were then mounted in epoxy and polished before
153 the analysis. Cathodoluminescence (CL) imaging was performed (with 10 kV
154 acceleration voltage) to reveal zircon zoning textures and zircon-hosted apatite
155 inclusions.

156 **4.2 Apatite mineralogy**

157 CL imaging and *in situ* element mapping were carried out at the iCRAG Lab in
158 Trinity College Dublin, Ireland. Samples were first coated with 12 nm of carbon
159 before being introduced to a TESCAN S8000 field emission scanning electron
160 microscope (FE-SEM) operating with TESCAN Essence software platform (2018).
161 The SEM was used for imaging and performing a fully quantitative energy dispersive
162 x-ray spectroscopy (EDX) chemical analysis of the apatites. The instrument is
163 equipped with Bright Beam SEM column technology, backscatter electron (BSE)
164 imaging, colour CL detectors, and four Oxford Instruments X-Max 170 mm^2
165 detectors, with AZtec software version 5.1 used to interpret the EDX results. The CL
166 imaging was conducted on carbon-coated thin sections using a colour
167 cathodoluminescence detector at an acceleration voltage of 15 kV, a beam current of
168 3nA, a working distance of 15 mm, and an image scanning speed of 320 μs per pixel.
169 The EDX analysis was carried out with an acceleration voltage of 20 kV, a beam
170 current of 3 nA, and a working distance of 15 mm.

171 **4.3 Electron probe microanalysis**

172 *Apatite inclusions*

173 Before the geochemical analysis, we observed the sample and crystal texture
174 using an optical microscope and BSE imaging. The BSE imaging was conducted on
175 carbon-coated thin sections, using an accelerating voltage of 15 kV. Only the
176 inclusion-free, euhedral plagioclase-/biotite-hosted apatite inclusions and
177 groundmass-hosted apatite grains with homogeneous or zoned texture under BSE
178 imaging were selected for further study. Cathodoluminescence was conducted on the
179 apatite-host zircon to reveal the zircon internal texture. The zircon grains were briefly
180 polished before analysing the apatite inclusions to mitigate any potential beam
181 damage.

182 Major element compositions of the apatite inclusions were determined on a
183 JEOL JXA-8100 electron probe microanalyser (EPMA) at the State Key Laboratory
184 for Mineral Deposits Research, Nanjing University (China). Analysis was conducted
185 under 15 kV, 20 nA, and 2 μm beam size to generate sufficient counts to quantify the
186 low Cl content in the tiny apatite inclusions. Although these analytical conditions risk
187 minor electron-beam-induced sample damage (Goldoff et al., 2012; Stock et al., 2015;
188 Stormer et al., 1993), F and Cl were analysed first using shorter analysis times to
189 minimise this effect. The peak/background elemental counting times were
190 10/5 s for P, Ca, Cl and F, 20/10 s for Si. The standards used for the analysis included
191 the Durango apatite for Ca, P, and F, almandine for Si, barite for S, and tugtupite for
192 Cl. Previous studies have revealed the time-dependent variation in apatite halogen X-
193 ray counts during EPMA analysis (Goldoff et al., 2012; Stock et al., 2015). The effect
194 is most pronounced when the electron beam is oriented parallel to the crystallographic
195 c-axis, whereas it is minimal when the beam is parallel to the a- or b-axis (Goldoff et
196 al., 2012; Stock et al., 2015). The grains whose c-axis is parallel to the beam were

197 discarded to minimise the problem induced by the apatite anisotropy. We discarded
198 the apatite grains with a hexagonal symmetry (whose c-axis is likely beam-parallel;
199 crystals marked with white circles in Fig. 4b) and selected only the elongated apatite
200 grains (whose c-axis is likely beam-perpendicular; crystals marked with yellow, red,
201 and green circles in Fig. 4b). Analytical accuracy is <1% for P, <2% for Ca and F, and
202 <5% for Cl. Relative precision, quantified through repeated analyses of the
203 Wilberforce apatite, is $\pm 2\%$ for Ca, P, and F and $\pm 4\%$ for Cl (Table DR 1). The mole
204 fractions of fluorapatite and chlorapatite are calculated directly from the concentration
205 of F and Cl, with the mole fraction of hydroxyl-apatite (apatite OH content) estimated
206 using the approach in Ketcham (2015).

207 *Biotite and plagioclase phenocrysts*

208 Major element compositions of the apatite-hosting biotite and plagioclase were
209 analysed on a JXA-8230 EMPA at the Key Laboratory of Mineralogy and
210 Metallogeny (KLMM), Guangzhou Institute of Geochemistry, Chinese Academy of
211 Science (GIG CAS). The analysis was carried out using a 15 kV accelerating
212 voltage, 20 nA probe current, and 1 μm beam diameter. Peak/background counting
213 times are 20/10 s for Si, Al, Mg, Fe, and Ti, 10/5 s for K, Na, F, and Cl, 40 s for Mn,
214 and 20 s for Ca. The calibration standards include biotite for Si, magnetite for Fe,
215 olivine for Mg, almandine for Al, rutile for Ti, rhodonite for Mn, orthoclase for
216 K, albite for Na, Cr-diopside for Ca, BaF_2 for F, and tugtupite for
217 Cl. ZAF (Z: atomic number; A: absorption; F: fluorescence) calibration procedures we
218 re used to reduce the matrix effect.

219 **4.4 Laser ablation inductively coupled plasma mass spectrometry (LA-ICP-MS)** 220 **analysis**

221 Trace element contents of zircon were analysed on an ELEMENT XR (Thermo
222 Fisher Scientific) ICP-SF-MS coupled with a 193-nm (ArF) Resonetics RESolution
223 M-50 laser ablation system at GIG CAS. The analysis consisted of a 33 μm laser spot
224 size with a repetition rate of 5 Hz and an energy fluence of 4 J/cm^2 . NIST SRM 610
225 glass (Jochum et al., 2011; Pearce et al., 1997) and Temora zircon (Black et al., 2003)
226 standards were used for external calibration. A detailed analytical procedure is
227 described by Zhang et al.(2019).

228 We used LA-ICP-MS to analyse the apatite trace element contents at the School
229 of Resources and Environmental Engineering, Hefei University of Technology, using
230 an Agilent 7900 ICP-MS coupled with a 193-nm (ArF) Analyte HE laser-ablation
231 system. The analysis used a 30 μm beam with a repetition rate of 8 Hz and an energy
232 fluence of 4 J/cm^2 . NIST SRM 610, NIST SRM 612, and BCR-2G were used for
233 external standards. The Ca concentration determined by EMPA was used as the
234 internal standard. The offline data processing, time-drift correction, and quantitative
235 calibration of both the zircon and apatite data were carried out with the
236 ICPMSDataCal program (Liu et al., 2008).

237 **5. Results**

238 **5.1 Host mineral compositions and saturation temperature**

239 Biotite phenocrysts are euhedral and un-zoned (Fig. 3d) and have near-
240 homogeneous intergrain compositions (Fig. DR2). They have high Mg# (molar
241 $\text{Mg}/(\text{Mg}+\text{Fe})$: 0.69–0.72; Table DR3) and TiO_2 content (3.65–4.82 wt.%), indicating
242 a magmatic origin (Rasmussen and Mortensen, 2013) despite weak alteration.
243 Following Henry et al. (2005), we calculated the Ti-in-biotite saturation temperature
244 to be 759–789 $^{\circ}\text{C}$ (mean= 777 \pm 8 $^{\circ}\text{C}$, n=25; Table DR3). The Al-in-biotite barometer
245 for granites was used to estimate the crystallisation pressure (Uchida et al., 2007). The

246 pressures at the time of biotite crystallisation are 167–249 MPa (mean 205 ± 24 MPa).
247 The water solubility at this pressure was estimated with the equation by Tattitch et al.
248 (2021), which yielded 6.14 ± 0.49 wt.% ($n = 25$; Table DR3).

249 Plagioclase phenocrysts are euhedral and concentric oscillatory-zoned (Fig. 3a,
250 3c). They are andesine in composition, with An values ($100 \times \text{molars CaO}/(\text{CaO} +$
251 $\text{Na}_2\text{O} + \text{K}_2\text{O})$) of 37–46 (Table DR4), and display a progressive decrease from core
252 (An_{41-46}) to rim (An_{37-43}). The An in plagioclase is sensitive to the magmatic water
253 content and temperature, but less sensitive to pressure (Water and Lange, 2015). The
254 plagioclase hygrometer is used to estimate the magmatic water content at the time of
255 plagioclase crystallisation (Water and Lange, 2015). Since the plagioclase and the
256 biotite phenocrysts should have both crystallised in the magma chamber, the biotite
257 thermobarometer (205 MPa) and the Ti-in-biotite saturation temperature (777 °C)
258 were used to estimate the water content. The average magmatic water content for the
259 sample was estimated to be 6.62 ± 0.07 wt.% ($n = 16$), similar to the results from
260 biotite.

261 Our zircon samples show oscillatory zoning in CL images (Fig. 4b). They have
262 ΣREE and Y concentrations of 727 to 1339 ppm (Table DR2) with strong LREE
263 depletion and positive Ce anomalies typical of igneous zircons (Fig. DR1), indicating
264 a lack of hydrothermal alteration (Fu et al., 2009; Hoskin, 2005). Following Loucks et
265 al. (2020), we calculated the Ti-in-zircon saturation temperature with pressure
266 correction. As quartz is a matrix constituent in the granodiorite porphyry, this
267 suggests that $\alpha\text{SiO}_2 = 1$. The presence of titanite indicates that αTiO_2 should be ~ 0.7
268 (Chelle-Michou et al., 2014). In our calculation, we used 1.0 and 0.7 for αSiO_2 and
269 αTiO_2 , respectively. The estimated pressure for correction is 205 MPa (Table DR3,
270 Uchida et al., 2007). The analysis yielded apparent temperatures of 722–818 °C

271 (mean $766 \pm 29^\circ\text{C}$, $n = 13$; Table DR2), broadly consistent with the Ti-in-zircon
272 saturation temperatures reported from other porphyry deposits (e.g., $750\text{-}650^\circ\text{C}$ at
273 Bajo da la Alumbreira (Argentina); Buret et al., 2016; $850\text{-}700^\circ\text{C}$ at Yanacocha
274 (Puru), and Yerington (Nevada); Dilles et al., 2015). The zircon oxybarometer in
275 Loucks et al. (2020) was used to calculate the oxygen fugacity of the magma, which
276 yielded $\Delta\text{FMQ} + 0.9$ to $\Delta\text{FMQ} + 1.6$ (mean = $\Delta\text{FMQ} + 1.2$, $n = 13$).

277 **5.2 Cathodoluminescence features and Cl distribution**

278 The magmatic apatite grains in groundmass (Fig. 5a-c), biotite phenocryst (Fig.
279 5d-f), and plagioclase phenocryst (Fig. 5g-i) are texturally homogeneous under BSE
280 imaging and display pink to purple luminescence under CL imaging. Some grains
281 contain brown luminescence patches (Fig. 5b). The unaltered magmatic apatite grains
282 consistently show a homogeneous intragrain Cl concentration (Fig. 5c, f, and i),
283 regardless of their luminescence.

284 The altered apatite grains are characterized by containing fluid inclusions or
285 monazite inclusions and voids in BSE images (Fig. 5j), and complex textures under
286 the CL imaging (Fig. 5k). They consist of the remnants of magmatic apatite with
287 brown or pink luminescence, and the hydrothermal apatite with blue-grey
288 luminescence (Fig. 5k). The hydrothermal apatite form euhedral rims with light-blue
289 luminescence, overgrown on a grey-dark luminescence core (Fig. 5k). Monazite
290 inclusions in the grey-dark luminescence core indicate a fluid-coupled dissolution-
291 reprecipitation process within apatite during the alteration (Harlov et al., 2002; Harlov
292 and Förster, 2003). Element distribution in the altered apatite shows a sharp
293 compositional boundary, with the hydrothermal replaced/altered parts having a much
294 lower Cl content than the magmatic apatite remnants (Fig. 5l). This reflects the

295 interaction with hydrothermal fluids where Cl partitions into the fluid phase (Webster
296 et al., 2009).

297 **5.3 Apatite trace element composition**

298 Trace element composition of 17 unaltered magmatic apatite grains (7 phenocryst-
299 host and 10 in groundmass) and 4 altered apatites measured by LA-ICP-MS are
300 shown in Fig. 6 and listed in Table DR5.

301 The 17 unaltered apatite in phenocrysts phases yield REE+Y contents of 3433-
302 5412 ppm (mean 4289 ppm, n = 7) and slight LREE-enriched patterns ((La/Yb)_N=
303 2.41-3.04) (Fig. 6). The apatite in the groundmass has REE+Y contents of 3017-6024
304 ppm, (mean 4422 ppm, n = 10) and (La/Yb)_N= 2.43-3.08, comparable to those of the
305 apatite in phenocrysts.

306 The altered apatite has much lower REE+Y contents (449-1482 ppm) with higher
307 (La/Yb)_N (5.04-16.1) than those of the unaltered apatite (Fig. 6). This composition is
308 consistent with the altered apatite in other porphyry systems (Bouzari et al., 2016),
309 indicating REE dissolution and remobilisation by the hydrothermal fluids.

310 **5.4 Apatite volatile compositions**

311 The EPMA volatile element compositions of the apatite inclusions in zircon
312 microphenocrysts, apatite inclusions in phenocryst phases, and apatite in the
313 groundmass are summarised in Table 1, shown in Fig. 7, and detailed in Table DR6-
314 DR8.

315 ***Apatite inclusions in zircon microphenocrysts***

316 We further divided the zircon-hosted apatite inclusions into three textural sub-
317 groups (Fig. 4b): (1) apatite fully enclosed in the zircon core; (2) apatite fully
318 enclosed in the zircon rim; (3) apatite partially enclosed in zircon. In total, we
319 analysed 93 apatite inclusions in 25 zircons, and the results are listed in Table DR6.

320 Zircon-hosted apatite inclusions display significant intragrain variation in their
321 halogen contents (Fig. 7; Table 1).
322 Apatite from the zircon core has 0.78–1.51 wt.% (mean 1.05 wt.%, n = 15) F,
323 1.40–2.72 wt.% (mean 1.96 wt.%) Cl, and 1.12–1.79 wt.% (mean 1.38 wt.%) OH.
324 This equates to X_F^{Ap}/X_{OH}^{Ap} , X_{Cl}^{Ap}/X_{OH}^{Ap} , and X_F^{Ap}/X_{Cl}^{Ap} ratios of 0.4–1.2, 0.4–1.0, and
325 0.5–1.8, respectively (where X_F^{Ap} , X_{Cl}^{Ap} , and X_{OH}^{Ap} are mole fractions of F, Cl, and OH
326 in apatite, respectively).

327 Apatite from the zircon rim has slightly higher F (0.67–2.61 wt.%, mean 1.20
328 wt.%, n = 58), similar Cl (0.20–2.97 wt.%, mean 1.98 wt.%), and lower OH (0.69–
329 1.65 wt.%, mean 1.20 wt.%) contents than apatite from the zircon core. Their
330 X_F^{Ap}/X_{OH}^{Ap} , X_{Cl}^{Ap}/X_{OH}^{Ap} , and X_F^{Ap}/X_{Cl}^{Ap} ratios are of 0.4–3.3, 0.1–1.5, and 0.5–21,
331 respectively.

332 Apatite partly enclosed by zircon has higher F content (1.44–2.65 wt.%, mean
333 1.94 wt.%, n = 17), lower Cl (0.41–1.93 wt.% mean 1.21 wt%), and lower OH
334 contents (0.72–1.44 wt.%, mean 0.97 wt%) than apatite fully enclosed by zircon.
335 Their X_F^{Ap}/X_{OH}^{Ap} , X_{Cl}^{Ap}/X_{OH}^{Ap} , and X_F^{Ap}/X_{Cl}^{Ap} ratios are 0.9–3.2, 0.2–1.0, and 1.5–12.1,
336 respectively.

337 ***Apatite inclusions in phenocryst phases***

338 We analysed 41 apatite inclusions from 13 biotite phenocrysts and 18 apatite
339 inclusions from 8 plagioclase phenocrysts (Fig. 7 and Table DR7). These apatite
340 inclusions are all fully enclosed in their host phenocrysts. Apatite from the biotite
341 phenocrysts exhibits a more restricted compositional range than the zircon-hosted
342 inclusions, with 1.85–3.45 wt.% (mean 2.26 wt.%) F, 0.20–1.45 wt.% (mean 1.22
343 wt.%) Cl, and 0.07–1.01 wt.% (mean 0.67 wt.%) OH. This equates to X_F^{Ap}/X_{OH}^{Ap} ,

344 X_{Cl}^{Ap}/X_{OH}^{Ap} , and X_F^{Ap}/X_{Cl}^{Ap} ratios of 1.7–38, 0.4–9.2, and 2.5–32, respectively. Apatite
345 from the plagioclase phenocrysts has a volatile composition similar to those for
346 apatite hosted by biotite, with 2.13–3.35 wt.% (mean 2.64 wt.%) F, 0.18–1.47 wt.%
347 (mean 0.87 wt.%) Cl, and 0.06–0.84 wt.% (mean 0.49 wt.%) OH contents. This
348 equates to X_F^{Ap}/X_{OH}^{Ap} , X_{Cl}^{Ap}/X_{OH}^{Ap} , and X_F^{Ap}/X_{Cl}^{Ap} ratios of 2.4–49.0, 0.15–5.4, and 3.1–
349 35, respectively.

350 *Apatite crystals in groundmass*

351 We analysed 49 apatite grains in the groundmass (Table DR8). They have 1.92–
352 3.39 wt.% (mean 2.59 wt.%) F, 0.15–1.55 wt.% (mean 1.07 wt.%) Cl, and 0.04–0.87
353 wt.% (mean 0.44 wt.%) OH. This equates to X_F^{Ap}/X_{OH}^{Ap} , X_{Cl}^{Ap}/X_{OH}^{Ap} , and X_F^{Ap}/X_{Cl}^{Ap}
354 ratios of 2.1–78.8, 0.1–18.4, and 2.3–37.5, respectively.

355 **6. Discussion**

356 **6.1 Apatite origin and textural constraints on the timing of apatite entrapment**

357 Porphyry mineralization accompanies hydrothermal alteration, which may alter
358 the magmatic apatite and modify its geochemical composition (Bouzari et al., 2016;
359 Xing et al., 2020). Therefore, only the primary apatite free from alteration would
360 preserve the magmatic volatile record. Altered apatite is usually depleted in Mn, REE,
361 and Y, and forms new REE phosphates (incl. monazite inclusions; Xing et al., 2019;
362 Bouzari et al., 2016), due to the coupled dissolution-reprecipitation mechanism
363 (Harlov et al., 2002; Harlov and Förster, 2003; Harlov et al., 2005). Since Mn and
364 REEs are the most common CL activators in apatite (Barbarand and Pagel, 2001;
365 Roeder et al., 1987), altered apatite usually shows replacement texture in CL images.
366 Moreover, altered apatite in the porphyry systems is characterised by extremely low

367 Cl contents regardless of alteration types (Bouzari et al., 2016) because Cl partitions
368 more strongly into fluids than apatite (Webster et al., 2009).

369 In our study, the textures and geochemical compositions of zircon, biotite, and
370 plagioclase phenocrysts indicate that these minerals are magmatic in origin and free of
371 or weakly affected by hydrothermal alteration (section 5.1). Thus, the apatite
372 inclusions in these minerals should be magmatic in origin and be isolated from
373 hydrothermal alteration. The magmatic apatite grains analysed are free of fluid
374 inclusions with homogeneous or zoned texture under BSE (Fig. 5a, d, g) and CL
375 imaging (Fig. 5b, e, h). Compositionally, the apatite grains analysed yielded Mn/Fe
376 >1 and much higher REE+Y contents (>3000 ppm) than those of the altered apatite
377 (<1000 ppm), further indicating that they are unaltered (Bouzari et al., 2016). Besides,
378 the apatite in our study yielded Cl contents > 0.1 wt.% and plot on a continuous
379 composition trend in the ternary F–Cl–OH plot (Fig. 7g). Such a compositional trend
380 is inconsistent with the low Cl content for the apatite altered by hydrothermal fluids
381 (Bouzari et al., 2016), which should have recorded the magmatic volatile evolution.

382 Since our apatite grains should record magmatic volatile compositions (either the
383 timing of entrapment or re-equilibration), compositional comparison of apatite with
384 different textures could provide relative temporal constraints on the magmatic volatile
385 evolution. Phenocrysts are crystallised in the magma chamber, whereas the
386 groundmass phases are formed by rapid crystallisation during the magma ascent or
387 degassing in the roof of the magma chamber (Burnham, 1967). Thus, unless their host
388 phenocrysts did not provide an effective barrier from re-equilibration, apatite
389 inclusions that are fully enclosed by phenocrysts should have recorded the volatile
390 composition of melt at an earlier stage compared with apatite in the groundmass,

391 which can re-equilibrate with their host magma (and the exsolved fluid) until a late
392 stage.

393 Some zircon microphenocrysts contain more than one apatite inclusion, which
394 may be fully or partially enclosed by the host zircon. The former may preserve a
395 record of melt volatile evolution, whereas the latter may record the volatile
396 equilibration with the ambient magma. For these zircons, we assume that apatite fully
397 enclosed in the zircon core was entrapped before those in the zircon rim, and that both
398 inclusion types would preserve the volatile record at the time of entrapment. In
399 contrast, apatite partly enclosed by a zircon microphenocryst was likely in contact
400 with the ambient melt until solidification and could re-equilibrate with volatiles from
401 a later-stage melt, similar to the case of groundmass apatite.

402 **6.2 Apatite compositional evolution in an H₂O-saturated porphyry magma** 403 **chamber**

404 As F, Cl, and OH are stoichiometric constituents in the crystal structure of
405 apatite, their crystal-melt partitioning is non-Nernstian and can be described by a
406 series of exchange reactions in the form:



408 where the superscripts denote apatite (Ap) and melt (M).

409 The equilibrium relationship between the volatile composition of apatite crystals
410 and their host melt can be expressed by K_D exchange equations of the form:

$$411 \quad K_{D(Cl-OH)}^{Ap-M}(P, T) = \frac{X_{Cl}^{Ap}}{X_{OH}^{Ap}} \times \frac{X_{OH}^M}{X_{Cl}^M} \quad (2)$$

412 where the exchange coefficients (K_D) are constant at a given pressure and
413 temperature (Piccoli and Candela, 1994). Equation 2 assumes that F–Cl–OH exchange
414 in apatite behaves as an ideal solid solution; although this may not be strictly true, it is

415 consistent with the available experimental data (see the discussion in Stock *et al.*
416 2018). A comparison of ideal vs non-ideal apatite thermodynamic models suggests
417 that any non-ideality must be small (Humphreys *et al.*, 2021).

418 Stock *et al.* (2016, 2018) proposed a thermodynamic model to calculate the
419 apatite compositional evolution during H₂O-undersaturated and H₂O-saturated
420 magmatic crystallisation by varying the modelling parameters (incl. crystal–melt and
421 fluid–melt volatile partition coefficients, initial melt volatile content, and melt H₂O
422 solubility). The modelling compositional trends can be compared with datasets of
423 natural apatite to determine whether the magma, the apatite crystallised from, was
424 H₂O-saturated.

425 Regarding our textural constraints, X_{Cl}^{Ap}/X_{OH}^{Ap} appears to decrease while X_F^{Ap}/X_{OH}^{Ap}
426 and X_F^{Ap}/X_{Cl}^{Ap} appears to increase during magma evolution, from apatite fully
427 enclosed by zircon (esp. apatite in the zircon core, which was isolated from the earlier
428 melt) to apatite partly enclosed by zircon (which re-equilibrated with the later melt)
429 (Fig. 7c, f). The compositional trajectory recorded by zircon-hosted apatite is
430 inconsistent with cooling at a constant melt composition, which would generate
431 a positive X_{Cl}^{Ap}/X_{OH}^{Ap} vs. X_F^{Ap}/X_{OH}^{Ap} correlation (Piccoli and Candela, 1994; Stock *et al.*,
432 2018). The compositional trajectory is also inconsistent with volatile-undersaturated
433 crystallisation models, which are characterised by decreasing X_F^{Ap}/X_{Cl}^{Ap} and away
434 from the F apex in the ternary F–Cl–OH plot during magma evolution (Stock *et al.*,
435 2018). This is because F partitions more strongly into common hydrous minerals (e.g.,
436 apatite, biotite, and amphibole) than Cl, while Cl partitions more strongly than OH
437 (i.e., $\bar{D}_F^{C/M} > \bar{D}_{Cl}^{C/M} > \bar{D}_{OH}^{C/M}$; Benard *et al.*, 2017; Li and Hermann, 2015; Mathez and
438 Webster, 2005; Van den Bleeken and Koga, 2015). This is especially true, if the Cl

439 partition coefficient between the mineral and the melt ($\bar{D}_{Cl}^{C/M}$) is extremely low, the
440 water under-saturated evolution would produce increasing X_{Cl}^{Ap}/X_{OH}^{Ap} with decreasing
441 X_F^{Ap}/X_{OH}^{Ap} and X_F^{Ap}/X_{Cl}^{Ap} , similar to the negative correlation trends observed in our
442 zircon-hosted apatite inclusions (Fig. 7c and 7f; Stock et al., 2018). However, this is
443 inconsistent with that of a porphyry magma, which should have a relatively high
444 $\bar{D}_{Cl}^{C/M}$ due to the crystallisation of abundant Cl-bearing biotite and amphibole
445 (Richards et al., 2012). Besides, the decreasing F and increasing Cl content of the
446 melts during water-undersaturated evolution with low $\bar{D}_{Cl}^{C/M}$ would drive apatite
447 compositionally away from the F apex and towards the Cl apex in F-Cl-OH space
448 (Stock et al., 2018), which is opposite to the trend shown by our samples (Fig. 7g).
449 Instead, the compositional trend of our apatite inclusions closely matches those of the
450 H₂O-saturated crystallisation models (Fig. 7g), where Cl is partitioned from the melt
451 into an exsolving vapour phase while F is retained in the felsic melt (Candela, 1986;
452 Cassidy et al., 2022; Doherty et al., 2014; Stock et al., 2018; Webster et al., 2009). As
453 the solubility of H₂O in a magmatic system is mainly pressure-dependent, the
454 trajectory of apatite volatile evolution should be different during isobaric and
455 polybaric (decompressed) H₂O-saturated crystallisation. After H₂O saturation in the
456 isobaric scenario (i.e., second boiling), the melt water concentration remains constant,
457 water is exsolved due to continuous crystallisation, and changes in apatite volatile
458 concentration are driven primarily by partitioning of Cl into the vapour phase. In the
459 F-Cl-OH ternary space (Fig. 7g), following H₂O-saturation under isobaric conditions,
460 apatite compositions would move directly towards the F–OH binary, as Cl is strongly
461 partitioned into the vapour, before moving towards the F apex (Stock et al., 2018).

462 After H₂O saturation in the polybaric scenario (i.e., first boiling), the melt H₂O
463 concentration drops due to its decreasing solubility during decompression. The Cl
464 partition coefficients for fluid-melt are pressure dependent (Tattitch et al., 2021) but
465 always larger than 1 in felsic melts (Aiuppa et al., 2009; Webster et al., 2009), thus
466 the melt Cl still partitions into the vapour phase. The apatite compositions are
467 influenced by the decrease of both H₂O and Cl in the melt. In the ternary F-Cl-OH
468 plot, following H₂O-saturation under polybaric conditions, the apatite compositions
469 would move closer to the F apex than the trends created by the isobaric scenario, as
470 the H₂O is extracted from the melt alongside Cl (Fig. 7g; Stock et al., 2018). The
471 pressure dependence of apatite–melt K_D values would be superimposed on these
472 compositional changes, but the variation caused by this dependence is expected to be
473 small over the normal crustal pressure range (Riker et al., 2018).

474 The apatite fully enclosed by zircon displays a steep drop in X_{Cl}^{Ap} at
475 approximately X_{OH}^{Ap} in the ternary F–Cl–OH plot (Fig. 7g), consistent with the
476 trajectories modelled by isobaric H₂O-saturated (the continuous lines in Fig. 7g) and
477 the slowly-decompressed H₂O-saturated crystallisation (red dashed line in Fig. 7g,
478 Stock et al., 2018). This indicates that the apatites were entrapped by zircons at
479 relatively constant magmatic H₂O content/solubility, which likely took place in the
480 magma chamber. Therefore, we suggest that the apatite grains fully enclosed by
481 zircons recorded the volatile exsolution in the magma chamber. The fertile Zijinsan
482 porphyry magma likely reached water saturation during/before zircon crystallisation
483 in the magma chamber.

484 An alternative explanation is that the compositional trends of apatite in zircons
485 are controlled by the assimilation of Cl-depleted or F-enriched material, which would

486 increase the apatite X_F^{Ap} and drive crystals towards higher X_F^{Ap}/X_{OH}^{Ap} and X_F^{Ap}/X_{Cl}^{Ap}
487 ratios. However, a large amount of Cl-depleted or F-enriched material would be
488 required to decrease the apatite X_{Cl}^{Ap} by 80% (according to our data) within the time
489 frame of zircon growth. Furthermore, the most probable Cl-depleted and F-enriched
490 endmember in the Zijinshan district is the Proterozoic sedimentary rocks. Zircon Hf
491 isotopic analysis of the Luoboling granodiorite porphyry indicated that their
492 assimilation was insignificant (Huang et al., 2018; Jiang et al., 2013; Li and Jiang,
493 2014). This further suggests that assimilation of Cl-depleted or F-rich materials is
494 unlikely the cause of decreasing X_{Cl}^{Ap} and X_{Cl}^{Ap}/X_{OH}^{Ap} , and increasing X_F^{Ap}/X_{OH}^{Ap} and
495 X_F^{Ap}/X_{Cl}^{Ap} in zircon hosted apatite.

496 The thermobarometer for the biotite (Uchida et al., 2007) indicates that the
497 pressure of the Zijinshan fertile magma chamber was ~205 MPa (eqv. ~6.8 km depth)
498 and comparable to those of most porphyry magma chambers around the world
499 (5~15km, Sillitoe, 2010). Since our fertile porphyry magma has achieved water
500 saturation in the chamber, the water solubility estimated by the pressure should
501 represent the water content (~6.14 wt.%). The result is close to the water content
502 estimated by the plagioclase phenocryst compositions (~ 6.62 wt.%). Both results
503 suggest that the fertile porphyry magma was characterized by a significantly higher
504 water content than the common arc magmas (~ 4 wt.%; Plank et al., 2013). The high-
505 water content should therefore be the key factor contributing to the water saturation in
506 the magma chamber at the time of the zircon-apatite crystallisation. Meanwhile, a
507 high magmatic water content is not unique for fertile porphyry systems. Similar
508 magmatic water contents (> 6 wt.%) have been reported in many subduction-related
509 porphyry ore systems, such as the Rio Blanco in Peru (Chen et al, 2022), and the

510 Santo Tomas II, Black Mountain, Clifton, and Bumolo in the Philippines (Huang et al,
511 2023a).

512 **6.3. Volatile re-equilibrium between non-zircon hosted apatite and the melt after**
513 **magma chamber exsolution**

514 Given that the Ti-in-biotite saturation temperatures (mean 777 ± 7 °C) are
515 similar with the Ti-in-zircon saturation temperatures (mean 766 ± 29 °C), and that
516 plagioclase likely reaches the liquidus substantially earlier than zircon, we would
517 expect the biotite and plagioclase phenocrysts hosted apatite inclusions to record a
518 period during magmatic volatile evolution that was simultaneous with or earlier than
519 that of the fully enclosed zircon-hosted apatite inclusions (i.e., equal or higher X_{OH}^{Ap}
520 and X_{Cl}^{Ap} , and lower X_F^{Ap}/X_{OH}^{Ap} and X_F^{Ap}/X_{Cl}^{Ap}). In fact, despite having some
521 compositional overlap with fully enclosed zircon-hosted inclusions, apatite inclusions
522 in the biotite and plagioclase phenocrysts extend to markedly higher X_F^{Ap}/X_{OH}^{Ap} (Fig.
523 8b) and X_F^{Ap}/X_{Cl}^{Ap} (Fig. 8e), and lower X_{Cl}^{Ap} and X_{OH}^{Ap} (Fig. 7g), similar to the apatite
524 partly enclosed by zircon or that in the groundmass (Fig. 7).

525 While groundmass apatite crystals may have grown from a late-stage melt,
526 after significant degassing and shortly before emplacement, we might expect
527 inclusions within phenocrysts and zircon microphenocrysts to preserve a volatile
528 record earlier in magmatic evolution, at or before their entrapment. Their
529 compositional correlation with groundmass crystals can be explained by diffusional
530 re-equilibration with the late-stage melt and exsolved fluid, which can occur within
531 days to months under magmatic conditions (Stock et al. 2016; Li et al, 2020). In the
532 case of zircon-hosted inclusions which were not fully enclosed by their host crystals,
533 diffusive re-equilibration is possible because crystals had not been isolated from their

534 host magma. In terms of inclusions within plagioclase and biotite phenocrysts, these
535 phases are weakly altered in our porphyry samples (Fig. 3), likely due to interaction
536 with exsolved Cl-rich magmatic fluids. This might have compromised them as an
537 inclusion host and permitted re-equilibration of apatite inclusions (Krause et al.,
538 2013).

539 The complexity of apatite volatile compositions in porphyry system might also
540 be explained by the slower cooling and the longer lifespan (100,000 to several million
541 years; Sillitoe, 2010) of the porphyry systems, which is long enough for volatile
542 diffusion to achieve re-equilibrium under high (magmatic) temperatures (Brenan,
543 1994; Costa et al., 2008; Costa et al., 2020). This is in contrast to previous analyses of
544 non-porphyry volcanic apatite inclusions, where common phenocrysts appear to be
545 reliable host phases, permitting apatite inclusions to retain a volatile record at their
546 time of entrapment (Stock et al., 2018). Nevertheless, our data indicate that zircon
547 could robustly shield the fully enclosed apatite inclusions from diffusive re-
548 equilibration in porphyry systems, allowing them to preserve their primary volatile
549 composition at the time of entrapment. This is consistent with the recent experimental
550 study, which indicates that zircon can resist alteration by Cl-rich fluids at magmatic
551 conditions (900°C and 1000 MPa; Harlov et al., 2023).

552 The steep decreases in X_{Cl}^{Ap} and X_{OH}^{Ap} between apatite inclusions which are
553 fully enclosed by zircon host crystals and those in other textural associations (i.e. all
554 of our crystals which are not fully enclosed within zircon; Fig. 7g) indicates a
555 substantial depletion of Cl in the melt by the exsolving H₂O-rich fluids. This is
556 consistent with the volatile compositions of the melt calculated to be in equilibrium
557 with the apatite crystals using the model Li and Costa (2020) (Fig. 8). Melt

558 equilibrium with zircon-hosted apatite has higher $\frac{X_{OH}^M}{X_F^M}$, $\frac{X_{Cl}^M}{X_F^M}$, and $\frac{X_{OH}^M}{X_{Cl}^M}$ than those in
559 equilibrium with apatite crystals in other textural associations, suggesting that the
560 zircon hosted crystals record an earlier stage in magmatic evolution, where the melt
561 had undergone less volatile degassing. Apatite inclusions within biotite and
562 plagioclase phenocrysts, apatite inclusions which are only partly enclosed by zircon,
563 and groundmass apatite crystals preserve a later-stage volatile record compared to
564 apatite inclusions which are fully enclosed in zircon (Fig. 9a), after significantly more
565 volatile exsolution in the magma chamber (Fig. 9b).

566 Previous experimental studies indicated that Cu in the melt partitions strongly
567 into the sulphide (Li and Audetat, 2012) and fluid phases (Zajacz et al., 2008). Our
568 porphyry magma is highly oxidized ($\sim \Delta FMQ+1.2$), where sulphate (S^{6+}) should be
569 the dominating sulphur phase (Jugo et al., 2009), and the fractionation of sulphides
570 should be depressed (e.g., Lynton et al., 1993; Ballard et al., 2002; Sun et al., 2014).
571 In such an oxidized environment, Cu and Mo readily form Cl-complexes and partition
572 into H_2O -rich fluids (Audétat, 2019; Audetat and Simon, 2012; Candela and Holland,
573 1986; Williams-Jones and Migdisov, 2014). Therefore, we suggest that, along with
574 the Cl, most of the Cu and Mo in the magma should have been extracted by the fluids
575 during the volatile exsolution in the magma chamber.

576 **7. Implications**

577 Previous research has suggested that volatile exsolution in magma chambers
578 controls the metal budgets of porphyry ores, based on the observation that fluid
579 inclusions, bulk ore, and volcanic gases have metal ratios comparable to those in the
580 sulfide melts (Halter et al., 2002; Nadeau et al., 2010; Rottier et al., 2019; Stavast et
581 al., 2006). Moreover, modeling studies indicated that volatile exsolution in magma

582 chambers would benefit the fluid-melt chemical equilibrium, thereby enhancing
583 extraction of the ore-forming materials (Cu, Mo, Cl, and S) from the melts (Candela,
584 1986, Huber et al., 2012).

585 Our results indicate the zircon-hosted apatite inclusions can provide a direct record
586 of the volatile evolution and exsolution in a porphyry magma chamber, and that their
587 water-saturated compositional patterns indicate that Cl and H₂O (and associated Cu and
588 Mo) were extracted from the melt by isobaric degassing (Fig. 9a). Besides, recent
589 research indicates that some other porphyry systems have achieved water saturation in
590 their magma chamber(s) at the time of zircon-apatite crystallisation, such as at the
591 Quellaveco porphyry deposit, Peru (Nathwani et al., 2023) and the Yulong porphyry
592 deposit, Tibet (Huang et al., 2023b). Since volatile exsolution in the magma chamber
593 is an essential prerequisite for porphyry ore magma fertility, zircon-hosted apatite with
594 water-saturated compositional patterns could be a novel mineral-geochemical indicator
595 for potential porphyry mineralization.

596 Our study also indicated that some resilient minerals, such as zircon, can shield
597 apatite inclusions from hydrothermal alteration and post-entrapment diffusion in the
598 porphyry system, whereas other minerals (e.g., plagioclase and biotite phenocrysts)
599 may not shield the apatite inclusions from the diffusive volatile re-equilibrium after
600 apatite entrapment due to the propensity for hydrothermal alteration, or volatile
601 diffusion at a magmatic temperature during an up to millions years' time window of
602 cooling in the porphyry system (Brenan, 1994). This contrasts with phenocryst-hosted
603 apatite inclusions in rapid cooling volcanic systems, which can retain the volatile
604 composition at the time of entrapment even when the melt inclusion record has been
605 reset by post-entrapment diffusive re-equilibration (Stock et al., 2016, 2018). Hence,
606 reconstruction of magmatic volatile compositions using apatite inclusions from

607 porphyry systems should be performed with caution, and post-entrapment re-
608 equilibrium with the melt or the exsolved magmatic fluids must be considered.

609 Finally, although the zircon can resist the Cl-rich fluid metasomatism in
610 porphyry systems, it can be altered, or replaced by another mineral in alkali- and F-
611 rich fluids at crustal temperature-pressure conditions (i.e. Harlov et al., 2023; Huang
612 et al., 2020). Therefore, the application of zircon-host apatite inclusions in other
613 magmatic-hydrothermal systems (such as the pegmatites and highly evolved granites)
614 should be performed with caution, and systemic mineralogical and geochemical
615 studies are necessary before interpreting data from these mineral inclusions.

616 **Acknowledgements**

617 The data of this work are available in the article and its online supplementary
618 material. This study was funded by the National Natural Science Foundation of China
619 (42072088) and the National Key R&D Program of China (2018YFA0702600). We
620 thank Changming Xing, Yonghua Cao and Wenlan Zhang for their help with the
621 electron microprobe analyses. We thank Daniel E. Harlov for handling the
622 manuscript, and Andreas Audétat and Chetan Nathwani for the constructive
623 suggestions, which helps to significantly improve the manuscript. WH acknowledges
624 the support from the China Scholarship Council (CSC) Scholarship (No.
625 202104910197). MS was supported by a Frontiers for the Future grant (20/FFP-
626 P/8895), co-funded by Science Foundation Ireland and Geological Survey Ireland. PG
627 was supported by SFI Research Centre for Applied Geosciences, Ireland (iCRAG,
628 13/RC/2092_2).

629

Figure Captions

630 **Figure 1** Geological map of the Zijinshan orefield (modified after Huang et al., 2018).

631

632 **Figure 2** Geological cross section of the Luoboling porphyry Cu-Mo deposit

633 (modified after Li and Jiang, 2017).

634

635 **Figure 3** BSE images showing (a) mineral assemblage of the Luoboling granodiorite

636 porphyry, (b) zircon in the groundmass, (c) zircon inclusion in plagioclase phenocryst,

637 (d) apatite inclusion enclosed by biotite phenocryst, (e) primary apatite in the

638 groundmass, and (f) altered apatite in the groundmass. Abbreviation: Anh =

639 anhydrite; Ap = apatite; Bi = biotite; Mon = monazite; Pla = plagioclase; Qtz =

640 quartz; Pl= plagioclase; Zr = zircon.

641

642 **Figure 4** Transmitted-light (a) and cathodoluminescence (b) microphotographs of

643 apatite inclusions enclosed by zircon. Abbreviations: AFIZC = apatite inclusions fully

644 enclosed by a zircon core; AFIZR= apatite fully enclosed by a zircon rim; APIZ =

645 apatite partially enclosed by zircon.

646

647 **Figure 5.** Apatite textural association under BSE imaging (left) and CL imaging

648 (middle) and EDS Cl distribution (right) in the Luoboling granodiorite porphyry.

649 Primary apatite in the groundmass (a-c), biotite phenocryst (d-f), and plagioclase

650 phenocryst (g-i) show homogeneous texture under BSE and CL imaging, with even Cl

651 distribution. Hydrothermally altered apatite from the groundmass in which monazite

652 inclusions formed (j). Complex replacement texture in CL (k). The altered part shows

653 a lower Cl content than the primary apatite (l). Abbreviation: Ap = apatite; Anh =

654 anhydrite; Bi = biotite; Cal= calcite; Kfs = K-feldspar; Nfs = Na-feldspar; Mon =
655 monazite; Pla = plagioclase.

656

657 **Figure 6** Chondrite-normalised rare earth elements (REEs) patterns for the apatite
658 inclusions in the Luoboling granodiorite porphyry. The normalising values are from
659 Sun and McDonough (1989).

660

661 **Figure 7** Scatter plots of apatite compositions in (a, b, and c) X_{Cl}^{Ap}/X_{OH}^{Ap} vs. X_F^{Ap}/X_{OH}^{Ap} ,
662 (d, e, and f) X_{Cl}^{Ap}/X_{OH}^{Ap} vs. X_F^{Ap}/X_{Cl}^{Ap} , and (g) ternary F–Cl–OH space. The insets in (c,
663 f, g) show modelled apatite compositional trajectories from Stock et al. (2018). Black
664 solid line shows one potential trajectory of apatite compositional evolution during
665 volatile-undersaturated crystallisation. Colored lines distinguish the volatile-saturated
666 models with $D_F^{f/m} = 0.7$, and $D_{Cl}^{f/m} = 50$ (dark blue), $D_{Cl}^{f/m} = 20$ (red), $D_{Cl}^{f/m} = 10$
667 (green), and $D_{Cl}^{f/m} = 4$ (orange). The line types illustrate the difference between
668 isobaric and polybaric conditions. Continuous lines show the trajectories modelled by
669 the isobaric volatile-saturated crystallization (with 0% water loss per unit
670 crystallisation); Dashed lines denote the trajectory of apatite compositional evolution
671 during decompression with 0.1 wt.% water loss per unit crystallization; Dotted line
672 shows a higher H₂O loss rate at 0.25 wt.% per unit crystallisation. Note that the fluids
673 and melts partition coefficients of F and Cl applied in the green lines ($D_{Cl}^{fluid/melt} = 10$
674 and $D_F^{fluid/melt} = 0.7$) are similar to the experimental results of the dacite melts at
675 similar pressure and temperature to our granodioritic porphyry ($D_{Cl}^{fluid/melt} = 11.1 \pm$
676 3.5 ; $D_F^{fluid/melt} = 0.8 \pm 0.8$ at 50-150 MPa and 800-1000 °C; Cassidy et al., 2022).

677

678 **Figure 8** Scatter plots of calculated volatile ratios equilibrated with apatites following
679 Li and Costa (2020). (a) X_{OH}^M/X_F^M vs. X_{Cl}^M/X_F^M , and (b) X_{OH}^M/X_{Cl}^M vs. X_{Cl}^M/X_F^M .
680 Symbol legend is the same as for Figure 7.

681

682 **Figure 9** Schematic diagram summarising the volatile evolution during porphyry Cu
683 ore formation, based on the apatite composition (modified after Richards, 2016). The
684 F–Cl–OH ternary diagram illustrates apatite composition changes during different
685 magmatic processes in the porphyry ore system. (a) Magma achieved volatile
686 saturation and began to generate separated fluid phases that extracted S, Cu, Mo, and
687 Cl from the magma chamber at a relatively steady pressure. The apatite grains
688 captured by plagioclase, biotite phenocrysts, and zircon at this stage should have
689 plotted on the compositional trends consistent with isobaric H₂O-saturated
690 crystallization; (b) The magma exsolved large amounts of fluids during its ascent and
691 emplacement, and caused the steep drop in the magma H₂O–Cl contents. The zircon
692 resisted the fluid metasomatism and the apatite grains fully enclosed by zircon cores
693 and rims preserved the primary volatile record of isobaric H₂O-saturated
694 crystallization. The reset of apatite inclusions (partly enclosed by zircon, in the
695 groundmass, and fully enclosed by the plagioclase and biotite phenocrysts) achieved
696 re-equilibrium with the post-exsolution melts, thereby falling on a compositional
697 trend toward the F apex in the F–Cl–OH ternary diagram.

698 Abbreviations: AFIZC = apatite inclusions fully enclosed by a zircon core; AFIZR=
699 apatite fully enclosed by a zircon rim; APIZ = apatite partially enclosed by zircon;
700 AFIB = apatite inclusions in biotite phenocryst; AFIP = apatite inclusions in
701 plagioclase phenocryst; AMG = apatite in the groundmass. Ap = apatite; Bio =
702 biotite; Pla = plagioclase; Kfs = K-feldspar; Qtz = quartz; Zr = zircon.

703

Tables

Table 1 Summarization of the volatile composition of apatite from the Luoboling granodiorite porphyry

Type	In zircon				In phenocryst phases						In groundmass					
	Zircon core		Zircon rim		Partly included		Biotite		Plagioclase		In Quartz		In K-feldspar		Intergranular	
Amount	15		58		17		41		18		21		14		14	
	range	avg.	range	avg.	range	avg.	range	avg.	range	avg.	range	avg.	range	avg.	range	ave.
F (wt.%)	0.78-1.51	1.05	0.67-2.61	1.2	1.44-2.65	1.94	1.85-3.45	2.26	2.13-3.35	2.64	1.95-2.97	2.53	2.03-3.39	2.63	1.92-3.03	2.58
Cl (wt.%)	1.40-2.72	1.96	0.20-2.97	1.98	0.41-1.93	1.21	0.20-1.45	1.22	0.18-1.47	0.87	0.43-1.47	1.16	0.18-1.40	1.1	0.15-1.55	1.09
OH(wt.%)*	1.12-1.79	1.38	0.69-1.65	1.21	0.72-1.44	0.97	0.07-1.01	0.67	0.06-0.84	0.49	0.11-0.83	0.45	0.04-0.87	0.44	0.03-0.83	0.45
X_F/X_{OH}	0.4-1.2		0.4-3.3		0.9-3.2		1.7-38		2.4-49.0		2.1-23.9		2.2-66.4		2.2-78.8	
X_{Cl}/X_{OH}	0.4-1.0		0.1-1.5		0.2-1.0		0.4-9.2		0.15-5.4		0.5-6.1		0.5-14.0		0.1-18.4	
X_F/X_{Cl}	0.5-1.8		0.5-21		1.5-12.1		2.5-32		3.1-35		2.7-13.0		2.7-34.9		2.3-37.5	

704

705 **Supplementary Materials**

706 **Figure DR1** Chondrite-normalized REE patterns of the zircon-hosted apatite
707 inclusions.

708 **Figure DR2** Chemical compositional diagrams of biotite phenocryst (after
709 Rieder *et al.*, 1998).

710 **Table DR1** Composition of the Wilberforce secondary apatite standard.

711 **Table DR2** Trace element composition and Ti-in-zircon temperature of zircon in
712 Luoboling granodiorite porphyry

713 **Table DR3** Major element composition of biotite phenocrysts from the
714 Luoboling porphyry Cu-Mo deposit

715 **Table DR4** Major element composition of plagioclase phenocrysts from the
716 Luoboling porphyry Cu-Mo deposit

717 **Table DR5** Trace element composition of primary and altered apatite grains in
718 the Luoboling granodiorite porphyry

719 **Table DR6** Composition of apatite inclusions in zircon from the Luoboling
720 porphyry Cu-Mo deposit

721 **Table DR7** Composition of primary apatite in the biotite and plagioclase
722 phenocrysts from the Luoboling porphyry Cu-Mo deposit

723 **Table DR8** Composition of primary apatite in the groundmass from the
724 Luoboling porphyry Cu-Mo deposit

725 **References cited**

726 Aiuppa, A., Baker, D.R., and Webster, J.D. (2009) Halogens in volcanic systems.
727 *Chemical Geology*, 263(1-4), 1-18.

728 Audétat, A. (2019) The Metal Content of Magmatic-Hydrothermal Fluids and Its
729 Relationship to Mineralization Potential. *Economic Geology*, 114(6), 1033-1056.

730 Audetat, A., and Simon, A.C. (2012) Magmatic controls on porphyry copper
731 genesis. Society of Economic Geologists, Littleton, CO, United States, United States.

732 Aud  tat, A., Simon, A.C., Hedenquist, J.W., Harris, M., and Camus, F. (2012)
733 Magmatic Controls on Porphyry Copper Genesis. Geology and Genesis of Major
734 Copper Deposits and Districts of the World: A Tribute to Richard H. Sillitoe, 16, p. 0.
735 Society of Economic Geologists.

736 Ballard, J.R., Palin, M.J., and Campbell, I.H. (2002) Relative oxidation states of
737 magmas inferred from Ce(IV)/Ce(III) in zircon: application to porphyry copper
738 deposits of northern Chile. Contributions to Mineralogy and Petrology, 144(3), 347-
739 364.

740 Barbarand, J., and Pagel, M. (2001) Cathodoluminescence study of apatite
741 crystals. American Mineralogist, 86(4), 473-484.

742 Bell, E.A., Boehnke, P., Harrison, T.M., and Wielicki, M.M. (2018) Mineral
743 inclusion assemblage and detrital zircon provenance. Chemical Geology, 477, 151-
744 160.

745 Bell, E.A., Boehnke, P., Hopkins-Wielicki, M.D., and Harrison, T.M. (2015)
746 Distinguishing primary and secondary inclusion assemblages in Jack Hills zircons.
747 Lithos, 234-235, 15-26.

748 Benard, A., Koga, K.T., Shimizu, N., Kendrick, M.A., Ionov, D.A., Nebel, O.,
749 and Arculus, R.J. (2017) Chlorine and fluorine partition coefficients and abundances
750 in sub-arc mantle xenoliths (Kamchatka, Russia): Implications for melt generation and
751 volatile recycling processes in subduction zones. Geochimica Et Cosmochimica Acta,
752 199, 324-350.

- 753 Black, L.P., Kamo, S.L., Allen, C.M., Aleinikoff, J.N., Davis, D.W., Korsch,
754 R.J., and Foudoulis, C. (2003) TEMORA 1: a new zircon standard for Phanerozoic U-
755 Pb geochronology. *Chemical Geology*, 200(1-2), 155-170.
- 756 Bouzari, F., Hart, C.J.R., Bissig, T., and Barker, S. (2016) Hydrothermal
757 Alteration Revealed by Apatite Luminescence and Chemistry: A Potential Indicator
758 Mineral for Exploring Covered Porphyry Copper Deposits. *Economic Geology*,
759 111(6), 1397-1410.
- 760 Boyce, J.W., and Hervig, R.L. (2008) Magmatic degassing histories from apatite
761 volatile stratigraphy. *Geology*, 36(1), 63-66.
- 762 Boyce, J.W., Tomlinson, S.M., McCubbin, F.M., Greenwood, J.P., and Treiman,
763 A.H. (2014) The Lunar Apatite Paradox. *Science*, 344(6182), 400-402.
- 764 Brenan J (1993) Kinetics of fluorine, chlorine and hydroxyl exchange in
765 fluorapatite. *Chemical Geology*, 110,195–210.
- 766 Bucholz, C.E., Gaetani, G.A., Behn, M.D., and Shimizu, N. (2013) Post-
767 entrapment modification of volatiles and oxygen fugacity in olivine-hosted melt
768 inclusions. *Earth and Planetary Science Letters*, 374, 145-155.
- 769 Buret, Y., von Quadt, A., Heinrich, C., Selby, D., Walle, M., and Peytcheva, I.
770 (2016) From a long-lived upper-crustal magma chamber to rapid porphyry copper-
771 emplacement: Reading the geochemistry of zircon crystals at Bajo de la Alumbrera
772 (NW Argentina). *Earth and Planetary Science Letters*, 450, 120-131.
- 773 Candela, P.A. (1986) Toward a Thermodynamic Model for the Halogens in
774 Magmatic Systems - an Application to Melt Vapor Apatite Equilibria. *Chemical*
775 *Geology*, 57(3-4), 289-301.

- 776 Candela, P.A., and Holland, H.D. (1986) A Mass-Transfer Model for Copper and
777 Molybdenum in Magmatic Hydrothermal Systems - the Origin of Porphyry-Type Ore-
778 Deposits. *Economic Geology*, 81(1), 1-19.
- 779 Cassidy, M., Iveson, A.A., Humphreys, M.C.S., Mather, T.A., Helo, C., Castro,
780 J.M., Ruprecht, P., Pyle, D.M., and EIMF. (2022) Experimentally derived F, Cl, and
781 Br fluid/melt partitioning of intermediate to silicic melts in shallow magmatic
782 systems. *American Mineralogist*, 107(10), 1825-1839.
- 783 Chelle-Michou, C., Chiaradia, M., Ovtcharova, M., Ulianov, A., and Wotzlaw,
784 J.F. (2014) Zircon petrochronology reveals the temporal link between porphyry
785 systems and the magmatic evolution of their hidden plutonic roots (the Eocene
786 Corocohuayco deposit, Peru). *Lithos*, 198, 129-140.
- 787 Chen, N., Meng, X.Y., Mao, J.W., and Xie, G.Q. (2022) Genetic Relationship
788 between Subduction of Slab Topographic Anomalies and Porphyry Deposit
789 Formation: Insight from the Source and Evolution of Rio Blanco Magmas. *Journal of*
790 *Petrology*, 63(6).
- 791 Chiaradia, M. (2021) Magmatic Controls on Metal Endowments of Porphyry Cu-
792 Au Deposits. *Society of Economic Geologists*.
- 793 Cooke, D.R., Hollings, P., and Walsh, J.L. (2005) Giant porphyry deposits:
794 Characteristics, distribution, and tectonic controls. *Economic Geology*, 100(5), 801-
795 818.
- 796 Costa, F., Dohmen, R., and Chakraborty, S. (2008) Time Scales of Magmatic
797 Processes from Modeling the Zoning Patterns of Crystals. *Reviews in Mineralogy and*
798 *Geochemistry*, 69(1), 545-594.

- 799 Costa, F., Shea, T., and Ubide, T. (2020) Diffusion chronometry and the
800 timescales of magmatic processes. *Nature Reviews Earth & Environment*, 1(4), 201-
801 214.
- 802 Dilles, J.H., Kent, A.J.R., Wooden, J.L., Tosdal, R.M., Koleszar, A., Lee, R.G.,
803 and Farmer, L.P. (2015) Zircon Compositional Evidence for Sulfur-Degassing from
804 Ore-Forming Arc Magmas. *Economic Geology*, 110(1), 241-251.
- 805 Doherty, A.L., Webster, J.D., Goldoff, B.A., and Piccoli, P.M. (2014)
806 Partitioning behavior of chlorine and fluorine in felsic melt-fluid(s)-apatite systems at
807 50 MPa and 850-950 degrees C. *Chemical Geology*, 384, 94-+.
- 808 Ferry, J.M., and Watson, E.B. (2007) New thermodynamic models and revised
809 calibrations for the Ti-in-zircon and Zr-in-rutile thermometers. *Contributions to*
810 *Mineralogy and Petrology*, 154(4), 429-437.
- 811 Fu, B., Mernagh, T.P., Kita, N.T., Kemp, A.I.S., and Valley, J.W. (2009)
812 Distinguishing magmatic zircon from hydrothermal zircon: A case study from the
813 Gidginbung high-sulphidation Au-Ag-(Cu) deposit, SE Australia. *Chemical Geology*,
814 259(3-4), 131-142.
- 815 Gaetani, G.A., O'Leary, J.A., Shimizu, N., Bucholz, C.E., and Newville, M.
816 (2012) Rapid reequilibration of H₂O and oxygen fugacity in olivine-hosted melt
817 inclusions. *Geology*, 40(10), 915-918.
- 818 Goldoff, B., Webster, J.D., and Harlov, D.E. (2012) Characterization of fluor-
819 chlorapatites by electron probe microanalysis with a focus on time-dependent
820 intensity variation of halogens. *American Mineralogist*, 97(7), 1103-1115.
- 821 Halter, W.E., Pettke, T., and Heinrich, C.A. (2002) The origin of Cu/Au ratios in
822 porphyry-type ore deposits. *Science*, 296(5574), 1844-1846.

- 823 Harlov, D.E., Andersson, U.B., Förster, H.-J., Nyström, J.O., Dulski, P., and
824 Broman, C. (2002) Apatite–monazite relations in the Kiirunavaara magnetite–apatite
825 ore, northern Sweden. *Chemical Geology*, 191(1), 47-72.
- 826 Harlov, D.E., and Förster, H.-J.r. (2003) Fluid-induced nucleation of (Y+REE)-
827 phosphate minerals within apatite: Nature and experiment. Part II. Fluorapatite.
828 *American Mineralogist*, 88(8-9), 1209-1229.
- 829 Harlov, D.E., Wirth, R., and Förster, H.-J. (2005) An experimental study of
830 dissolution–reprecipitation in fluorapatite: fluid infiltration and the formation of
831 monazite. *Contributions to Mineralogy and Petrology*, 150(3), 268-286.
- 832 Harlov, D.E., Anczkiewicz, R., and Dunkley, D.J. (2023) Metasomatic alteration
833 of zircon at lower crustal P-T conditions utilizing alkali- and F-bearing fluids: Trace
834 element incorporation, depletion, and resetting the zircon geochronometer.
835 *Geochimica et Cosmochimica Acta*, 352, 222-235.
- 836 Hedenquist, J.W., and Lowenstern, J.B. (1994) The Role of Magmas in the Formation of Hydrothermal Ore-Deposits.
837 *Nature*, 370(6490), 519-527.
- 838 Henry, D.J., Guidotti, C.V., and Thomson, J.A. (2005) The Ti-saturation surface
839 for low-to-medium pressure metapelitic biotites: Implications for geothermometry and
840 Ti-substitution mechanisms. *American Mineralogist*, 90(2-3), 316-328.
- 841 Hoskin, P.W.O. (2005) Trace-element composition of hydrothermal zircon and
842 the alteration of Hadean zircon from the Jack Hills, Australia. *Geochimica Et*
843 *Cosmochimica Acta*, 69(3), 637-648.
- 844 Huang, M.-L., Zhu, J.-J., Chiaradia, M., Hu, R.-Z., Xu, L.-L., and Bi, X.-W.
845 (2023a) APATITE VOLATILE CONTENTS OF PORPHYRY Cu DEPOSITS
846 CONTROLLED BY DEPTH-RELATED FLUID EXSOLUTION PROCESSES.
847 *Economic Geology*, 118(5), 1201-1217.

- 848 Huang, W.T., Li, J., Liang, H.Y., Wang, C.L., Lin, S.P., and Wang, X.Z. (2013)
849 Zircon LA-ICP-MS U-Pb ages and highly oxidized features of magma associated with
850 Luoboling porphyry Cu-Mo deposit in Zijinshan ore field, Fujian Province. *Acta*
851 *Petrologica Sinica*, 29(1), 283-293.
- 852 Huang, W.T., Liang, H.Y., Wu, L., Wu, J., Li, J., and Bao, Z.W. (2018)
853 Asynchronous formation of the adjacent epithermal Au-Cu and porphyry Cu-Mo
854 deposits in the Zijinshan orefield, southeast China. *Ore Geology Reviews*, 102, 351-
855 367.
- 856 Huang, W., Wu, J., Liang, H., Zhang, J., Ren, L., and Chen, X. (2020) Ages and
857 genesis of W-Sn and Ta-Nb-Sn-W mineralization associated with the Limu granite
858 complex, Guangxi, China. *Lithos*, 352-353, 105321.
- 859 Huang, W. T, Stock, M.J., Xia, X.-P., Sun, X., Cui, Z., Liuyun, O., Zhang, J.,
860 Chen, X., Zheng, Y., and Liang, H. (2023b) Determining the impact of magma water
861 contents on porphyry Cu fertility: Constraints from hydrous and nominally anhydrous
862 mineral analyses. *GSA Bulletin*.
- 863 Huber, C., Bachmann, O., Vigneresse, J.L., Dufek, J., and Parmigiani, A. (2012)
864 A physical model for metal extraction and transport in shallow magmatic systems.
865 *Geochemistry Geophysics Geosystems*, 13.
- 866 Humphreys, M.C.S., Smith, V.C., Coumans, J.P., Riker, J.M., Stock, M.J., de
867 Hoog, J.C.M., and Brooker, R.A. (2021) Rapid pre-eruptive mush reorganisation and
868 atmospheric volatile emissions from the 12.9 ka Laacher See eruption, determined
869 using apatite. *Earth and Planetary Science Letters*, 576.
- 870 Jiang, S.H., Liang, Q.L., Bagas, L., Wang, S.H., Nie, F.J., and Liu, Y.F. (2013)
871 Geodynamic setting of the Zijinshan porphyry–epithermal Cu–Au–Mo–Ag ore

872 system, SW Fujian Province, China: Constrains from the geochronology and
873 geochemistry of the igneous rocks. *Ore Geology Reviews*, 53, 287-305.

874 Jochum, K.P., Weis, U., Stoll, B., Kuzmin, D., Yang, Q.C., Raczek, I., Jacob,
875 D.E., Stracke, A., Birbaum, K., Frick, D.A., Gunther, D., and Enzweiler, J. (2011)
876 Determination of Reference Values for NIST SRM 610-617 Glasses Following ISO
877 Guidelines. *Geostandards and Geoanalytical Research*, 35(4), 397-429.

878 Jugo, P.J. (2009) Sulfur content at sulfide saturation in oxidized magmas.
879 *Geology*, 37(5), 415-418.

880 Kendall-Langley, L.A., Kemp, A.I.S., Hawkesworth, C.J., Craven, J., Talavera,
881 C., Hinton, R., Roberts, M.P., and Eimf. (2021) Quantifying F and Cl concentrations
882 in granitic melts from apatite inclusions in zircon. *Contributions to Mineralogy and*
883 *Petrology*, 176(7), 58.

884 Ketcham, R.A. (2015) Technical Note: Calculation of stoichiometry from EMP
885 data for apatite and other phases with mixing on monovalent anion sites. *American*
886 *Mineralogist*, 100(7), 1620-1623.

887 Krause, J., Harlov, D.E., Pushkarev, E.V., and Brüggemann, G.E. (2013) Apatite
888 and clinopyroxene as tracers for metasomatic processes in nepheline clinopyroxenites
889 of Uralian-Alaskan-type complexes in the Ural Mountains, Russian Federation.
890 *Geochimica et Cosmochimica Acta*, 121, 503-521.

891 Li, B., and Jiang, S.Y. (2014) A subduction-related metasomatically enriched
892 mantle origin for the Luoboling and Zhongliao Cretaceous granitoids from South
893 China: implications for magma evolution and Cu–Mo mineralization. *International*
894 *Geology Review*, 57(9-10), 1239-1266.

895 Li, B., Zhao, K.D., Zhang, Q., Xu, Y.M., and Zhu, Z.Y. (2015) Petrogenesis and
896 geochemical characteristics of the Zijinshan granitic complex from Fujian Province,
897 South China. *Acta Petrologica Sinica*, 31(3), 811-828.

898 Li, H.J., and Hermann, J. (2015) Apatite as an indicator of fluid salinity: An
899 experimental study of chlorine and fluorine partitioning in subducted sediments.
900 *Geochimica Et Cosmochimica Acta*, 166, 267-297.

901 Li, J.-X., Li, G.-M., Evans, N.J., Zhao, J.-X., Qin, K.-Z., and Xie, J. (2021)
902 Primary fluid exsolution in porphyry copper systems: evidence from magmatic apatite
903 and anhydrite inclusions in zircon. *Mineralium Deposita*, 56(2), 407-415.

904 Li, W.R., and Costa, F. (2020) A thermodynamic model for F-Cl-OH
905 partitioning between silicate melts and apatite including non-ideal mixing with
906 application to constraining melt volatile budgets. *Geochimica Et Cosmochimica Acta*,
907 269, 203-222.

908 Li, W.R., Chakraborty, S., Nagashima, K., and Costa, F. (2020) Multicomponent
909 diffusion of F, Cl and OH in apatite with application to magma ascent rates. *Earth and*
910 *Planetary Science Letters*, 550, 116545.

911 Li, Y., and Audétat, A. (2012) Partitioning of V, Mn, Co, Ni, Cu, Zn, As, Mo,
912 Ag, Sn, Sb, W, Au, Pb, and Bi between sulfide phases and hydrous basanite melt at
913 upper mantle conditions. *Earth and Planetary Science Letters*, 355-356, 327-340.

914 Loucks, R.R., Fiorentini, M.L., and Henriquez, G.J. (2020) New Magmatic
915 Oxybarometer Using Trace Elements in Zircon. *Journal of Petrology*, 61(3).

916 Lowenstern, J.B. (1994) Dissolved Volatile Concentrations in an Ore-Forming
917 Magma. *Geology*, 22(10), 893-896.

- 918 Lynton, S.J., Candela, P.A., and Piccoli, P.M. (1993) An experimental study of
919 the partitioning of copper between pyrrhotite and a high silica rhyolitic melt.
920 *Economic Geology*, 88(4), 901-915.
- 921 Mathez, E.A., and Webster, J.D. (2005) Partitioning behavior of chlorine and
922 fluorine in the system apatite-silicate melt-fluid. *Geochimica Et Cosmochimica Acta*,
923 69(5), 1275-1286.
- 924 McCubbin, F.M., and Jones, R.H. (2015) Extraterrestrial Apatite: Planetary
925 Geochemistry to Astrobiology. *Elements*, 11(3), 183-188.
- 926 Meng, X., Simon, A.C., Kleinsasser, J.M., Mole, D.R., Kontak, D.J., Jugo, P.J.,
927 Mao, J., and Richards, J.P. (2022) Formation of oxidized sulfur-rich magmas in
928 Neoproterozoic subduction zones. *Nature Geoscience*, 15(12), 1064-1070.
- 929 Nadeau, O., Williams-Jones, A.E., and Stix, J. (2010) Sulphide magma as a
930 source of metals in arc-related magmatic hydrothermal ore fluids. *Nature Geoscience*,
931 3(7), 501-505.
- 932 Nathwani, C.L., Large, S.J.E., Brugge, E.R., Wilkinson, J.J., Buret, Y., and Eimf.
933 (2023) Apatite evidence for a fluid-saturated, crystal-rich magma reservoir forming
934 the Quellaveco porphyry copper deposit (Southern Peru). *Contributions to Mineralogy
935 and Petrology*, 178(8), 49.
- 936 Pearce, N.J.G., Perkins, W.T., Westgate, J.A., Gorton, M.P., Jackson, S.E., Neal,
937 C.R., and Chenery, S.P. (1997) A compilation of new and published major and trace
938 element data for NIST SRM 610 and NIST SRM 612 glass reference materials.
939 *Geostandards Newsletter-the Journal of Geostandards and Geoanalysis*, 21(1), 115-
940 144.
- 941 Piccoli, P., and Candela, P. (1994) Apatite in Felsic Rocks - a Model for the
942 Estimation of Initial Halogen Concentrations in the Bishop Tuff (Long Valley) and

- 943 Tuolumne Intrusive Suite (Sierra-Nevada Batholith) Magmas. American Journal of
944 Science, 294(1), 92-135.
- 945 Piccoli, P.M., and Candela, P.A. (2002) Apatite in Igneous Systems. Reviews in
946 Mineralogy and Geochemistry, 48(1), 255-292.
- 947 Plank, T., Kelley, K.A., Zimmer, M.M., Hauri, E.H., and Wallace, P.J. (2013)
948 Why do mafic arc magmas contain ~4wt% water on average? Earth and Planetary
949 Science Letters, 364, 168-179.
- 950 Rasmussen, K.L., and Mortensen, J.K. (2013) Magmatic petrogenesis and the
951 evolution of (F:Cl:OH) fluid composition in barren and tungsten skarn-associated
952 plutons using apatite and biotite compositions: Case studies from the northern
953 Canadian Cordillera. Ore Geology Reviews, 50, 118-142.
- 954 Richards, J.P. (2011) Magmatic to hydrothermal metal fluxes in convergent and
955 collided margins. Ore Geology Reviews, 40(1), 1-26.
- 956 Riker, J., Humphreys, M.C.S., Brooker, R.A., and De Hoog, J.C.M. (2018) First
957 measurements of OH-C exchange and temperature-dependent partitioning of OH and
958 halogens in the system apatite–silicate melt. American Mineralogist, 103(2), 260-270.
- 959 Roeder, P.L., MacArthur, D., Ma, X.-P., Palmer, G.R., and Mariano, A.N. (1987)
960 Cathodoluminescence and microprobe study of rare-earth elements in apatite.
961 American Mineralogist, 72(7-8), 801-811.
- 962 Rottier, B., Audétat, A., Koděra, P., and Lexa, J. (2019) Origin and Evolution of
963 Magmas in the Porphyry Au-mineralized Javorie Volcano (Central Slovakia):
964 Evidence from Thermobarometry, Melt Inclusions and Sulfide Inclusions. Journal of
965 Petrology, 60(12), 2449-2482.
- 966 Sillitoe, R.H. (2010) Porphyry Copper Systems. Economic Geology, 105(1), 3-
967 41.

968 So, C.S., Zhang, D.Q., Yun, S.T., and Li, D.X. (1998) Alteration-mineralization
969 zoning and fluid inclusions of the high sulfidation epithermal Cu-Au mineralization at
970 Zijinshan, Fujian Province, China. *Economic Geology and the Bulletin of the Society*
971 *of Economic Geologists*, 93(7), 961-980.

972 Stavast, W.J., Keith, J.D., Christiansen, E.H., Dorais, M.J., Tingey, D.,
973 Larocque, A., and Evans, N. (2006) The fate of magmatic sulfides during intrusion or
974 eruption, Bingham and Tintic districts, Utah. *Economic Geology*, 101(2), 329-345.

975 Stock, M.J., Humphreys, M.C.S., Smith, V.C., Isaia, R., Brooker, R.A., and Pyle,
976 D.M. (2018) Tracking Volatile Behaviour in Sub-volcanic Plumbing Systems Using
977 Apatite and Glass: Insights into Pre-eruptive Processes at Campi Flegrei, Italy.
978 *Journal of Petrology*, 59(12), 2463-2491.

979 Stock, M.J., Humphreys, M.C.S., Smith, V.C., Isaia, R., and Pyle, D.M. (2016)
980 Late-stage volatile saturation as a potential trigger for explosive volcanic eruptions.
981 *Nature Geoscience*, 9(3), 249-U90.

982 Stock, M.J., Humphreys, M.C.S., Smith, V.C., Johnson, R.D., Pyle, D.M., and
983 EIMF. (2015) New constraints on electron-beam induced halogen migration in
984 apatite†. *American Mineralogist*, 100(1), 281-293.

985 Stormer, J.C., Pierson, M.L., and Tacker, R.C. (1993) Variation of F-X-Ray and
986 Cl-X-Ray Intensity Due to Anisotropic Diffusion in Apatite during Electron-
987 Microprobe Analysis. *American Mineralogist*, 78(5-6), 641-648.

988 Sun, W.D., Huang, R.F., Li, H., Hu, Y.B., Zhang, C.C., Sun, S.J., Zhang, L.P.,
989 Ding, X., Li, C.Y., Zartman, R.E., and Ling, M.X. (2015) Porphyry deposits and
990 oxidized magmas. *Ore Geology Reviews*, 65, 97-131.

991 Sun, W.D., Liang, H.Y., Ling, M.X., Zhan, M.Z., Ding, X., Zhang, H., Yang,
992 X.Y., Li, Y.L., Ireland, T.R., Wei, Q.R., and Fan, W.M. (2013) The link between

- 993 reduced porphyry copper deposits and oxidized magmas. *Geochimica Et*
994 *Cosmochimica Acta*, 103, 263-275.
- 995 Tattitch, B., Chelle-Michou, C., Blundy, J., and Loucks, R.R. (2021) Chemical
996 feedbacks during magma degassing control chlorine partitioning and metal extraction
997 in volcanic arcs. *Nature Communications*, 12(1).
- 998 Uchida, E., Endo, S., and Makino, M. (2007) Relationship between solidification
999 depth of granitic rocks and formation of hydrothermal ore deposits. *Resource*
1000 *Geology*, 57(1), 47-56.
- 1001 Van den Bleeken, G., and Koga, K.T. (2015) Experimentally determined
1002 distribution of fluorine and chlorine upon hydrous slab melting, and implications for
1003 F-Cl cycling through subduction zones. *Geochimica Et Cosmochimica Acta*, 171,
1004 353-373.
- 1005 Webster, J.D., Tappen, C.M., and Mandeville, C.W. (2009) Partitioning behavior
1006 of chlorine and fluorine in the system apatite-melt-fluid. II: Felsic silicate systems at
1007 200 MPa. *Geochimica Et Cosmochimica Acta*, 73(3), 559-581.
- 1008 Williams-Jones, A.E., and Migdisov, A.A. (2014) Experimental Constraints on
1009 the Transport and Deposition of Metals in Ore-Forming Hydrothermal Systems.
1010 *Building Exploration Capability for the 21st Century*(18), 77-95.
- 1011 Xing, K., Shu, Q., Lentz, D.R., and Wang, F. (2020) Zircon and apatite
1012 geochemical constraints on the formation of the Huojihe porphyry Mo deposit in the
1013 Lesser Xing'an Range, NE China. *American Mineralogist*, 105(3), 382-396.
- 1014 Zajacz, Z., Halter, W.E., Pettke, T., and Guillong, M. (2006) Determination of
1015 fluid/melt partition coefficients by LA-ICPMS analysis of co-existing fluid and
1016 silicate melt inclusions. *Geochimica Et Cosmochimica Acta*, 70(18), A730-A730.

- 1017 Zhang, J.J. (2013) Geology, exploration model and practice of Zijinshan ore
1018 concentrated area. *Mineral Deposits*, 32(4), 10.
- 1019 Zhang, L., Ren, Z.Y., Xia, X.P., Yang, Q., Hong, L.B., and Wu, D. (2019) In situ
1020 determination of trace elements in melt inclusions using laser ablation inductively
1021 coupled plasma sector field mass spectrometry. *Rapid Communications in Mass
1022 Spectrometry*, 33(4), 361-370.
- 1023 Zhong, J., Chen, Y.J., Pirajno, F., Chen, J., Li, J., Qi, J.P., and Li, N. (2014)
1024 Geology, geochronology, fluid inclusion and H–O isotope geochemistry of the
1025 Luoboling Porphyry Cu–Mo deposit, Zijinshan Orefield, Fujian Province, China. *Ore
1026 Geology Reviews*, 57, 61-77.

Figure 1

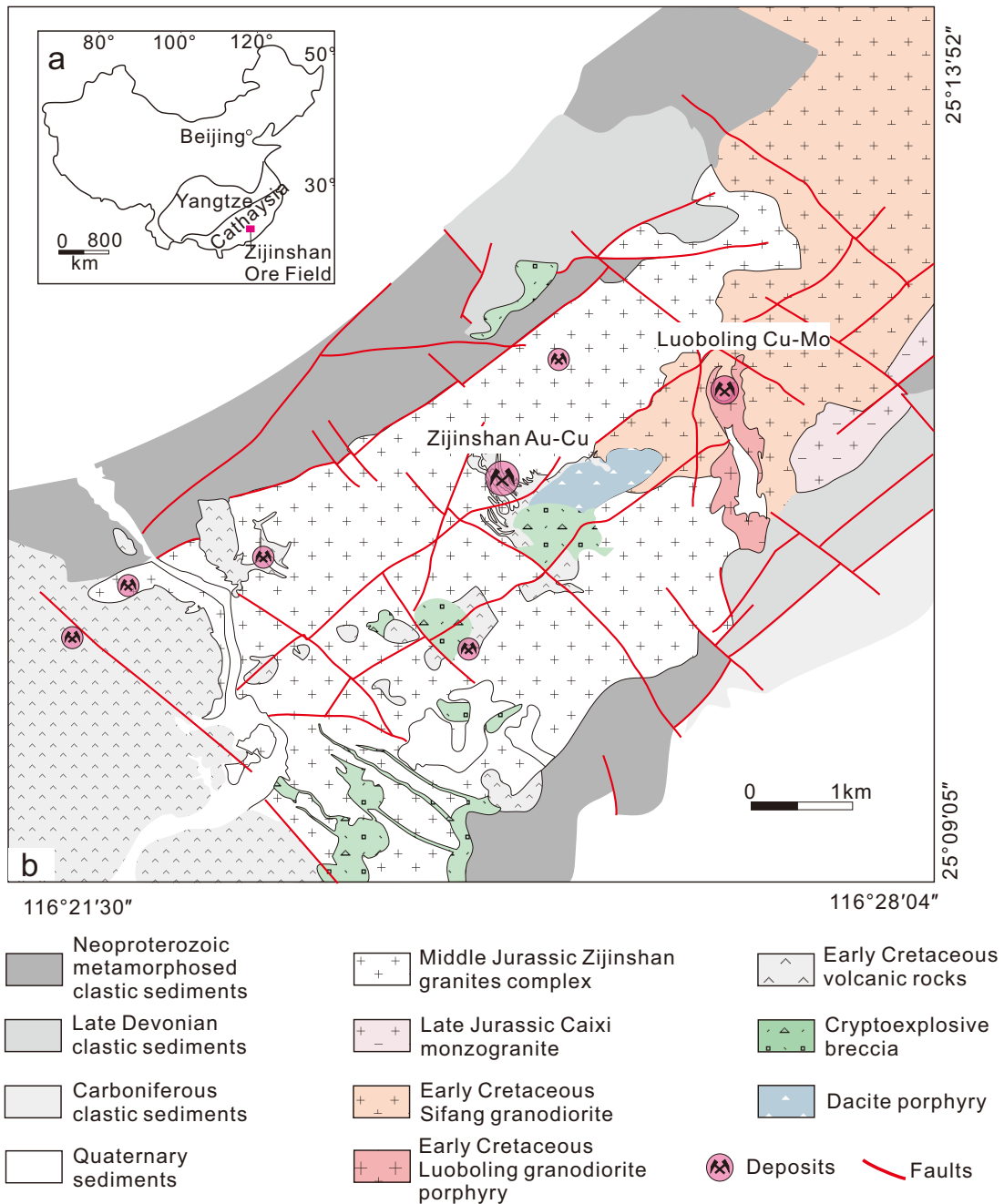


Figure 2

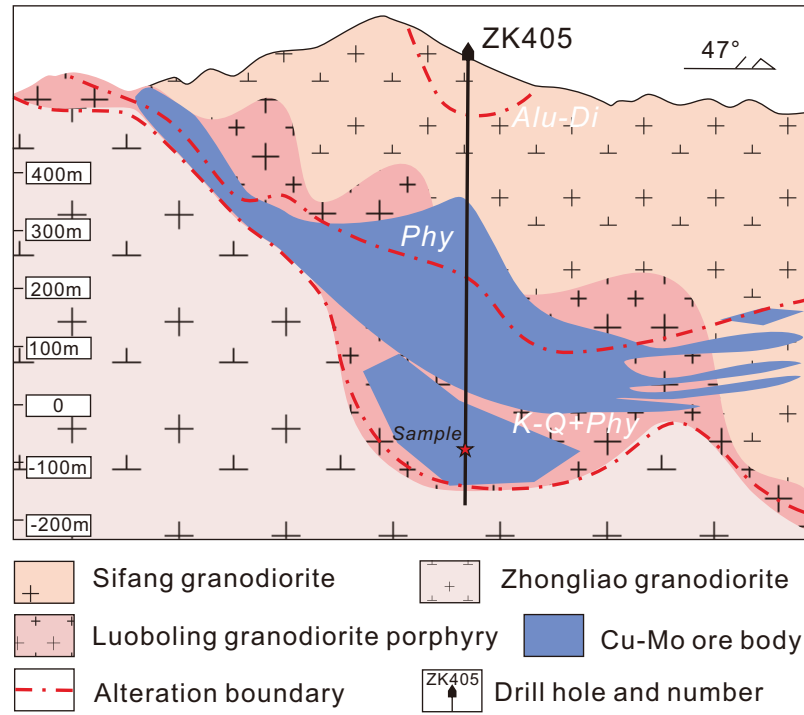


Figure 3

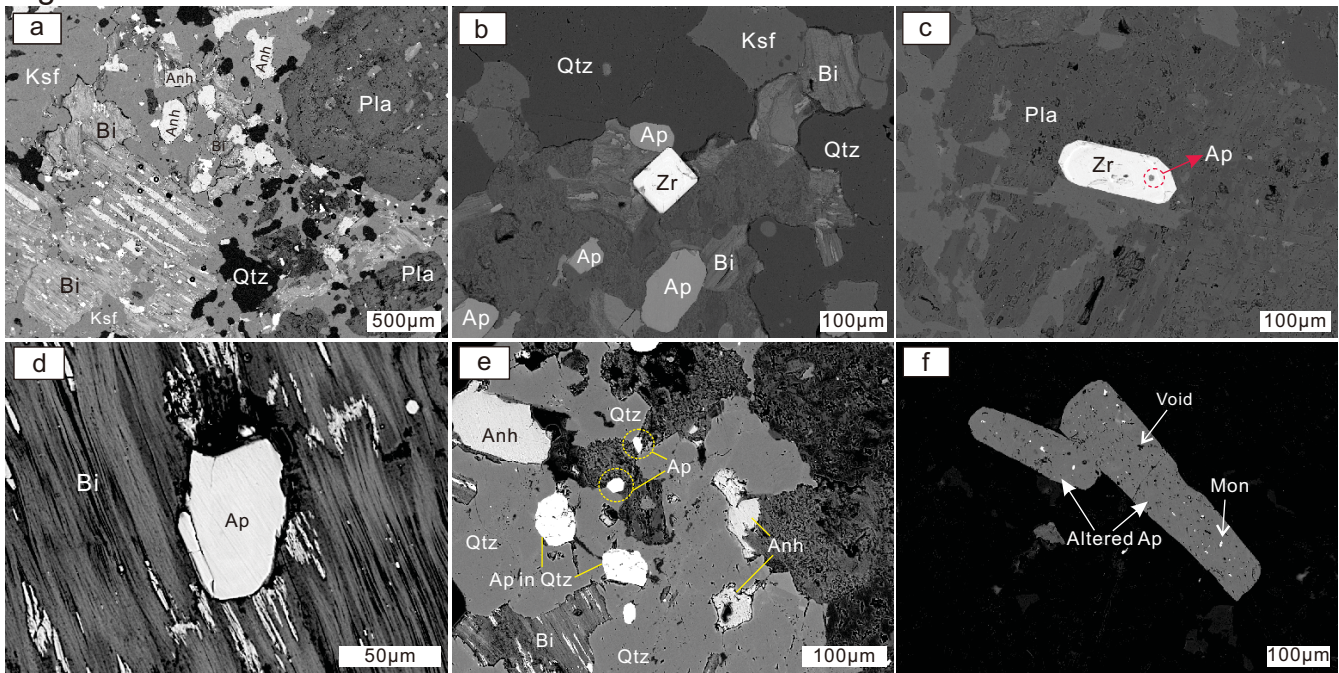


Figure 4

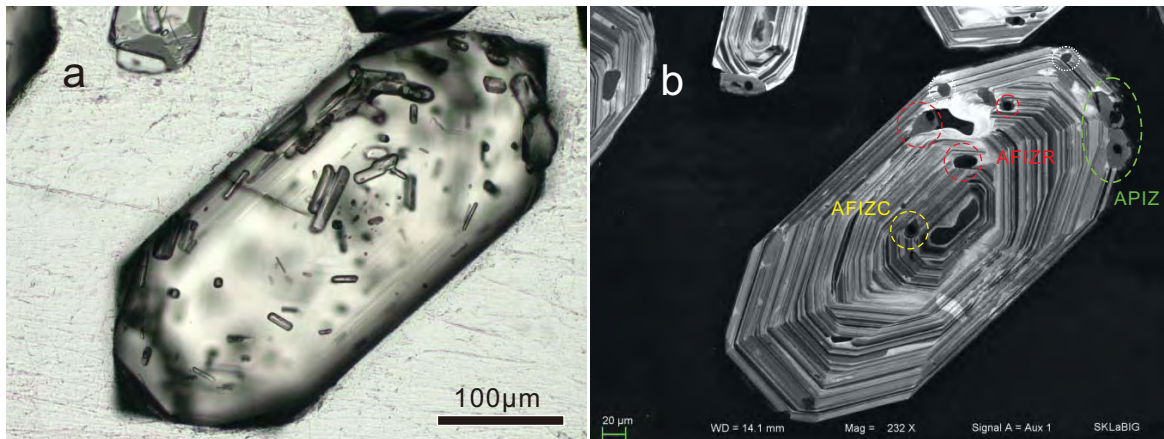


Figure 5

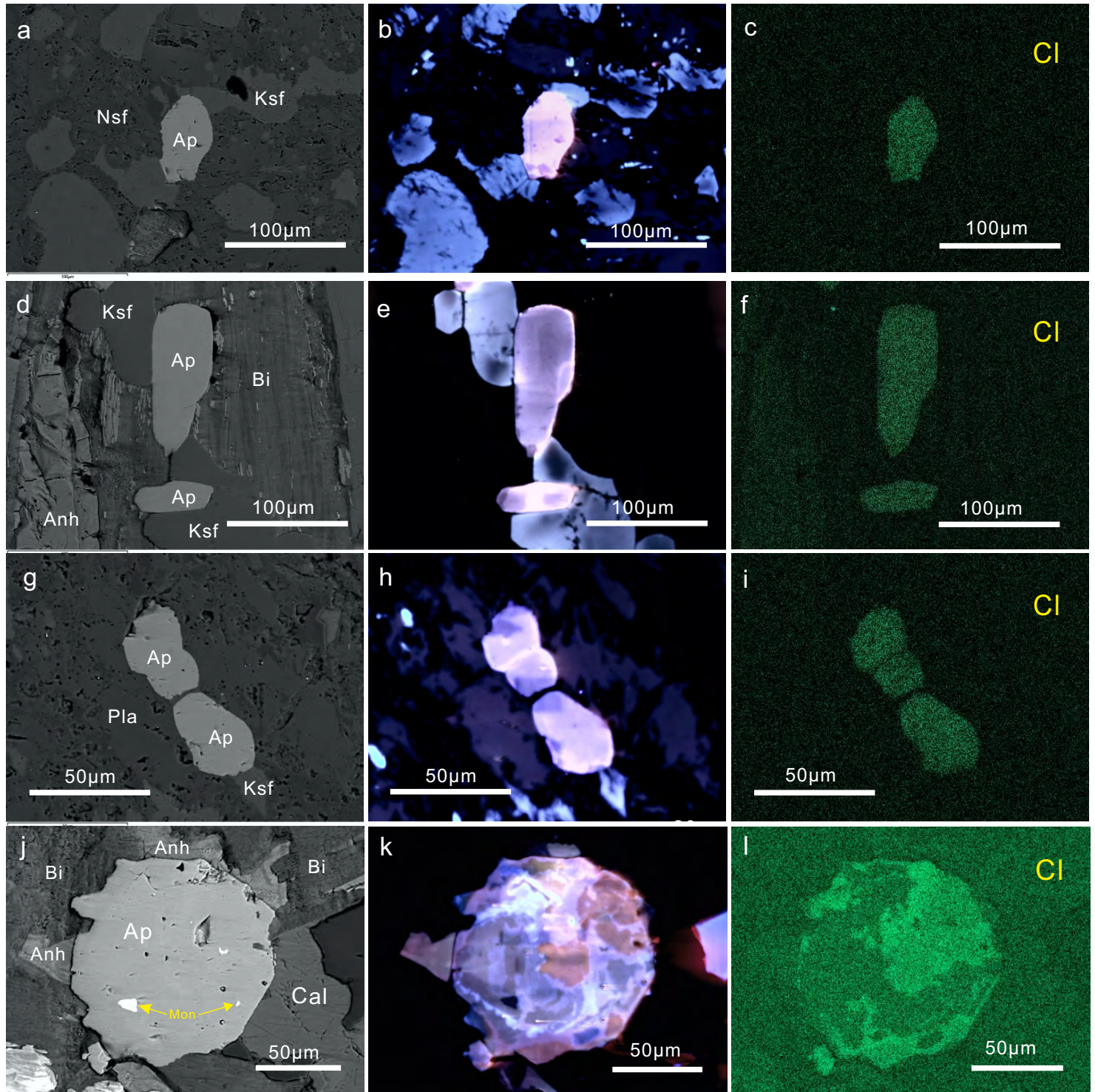


Figure 6

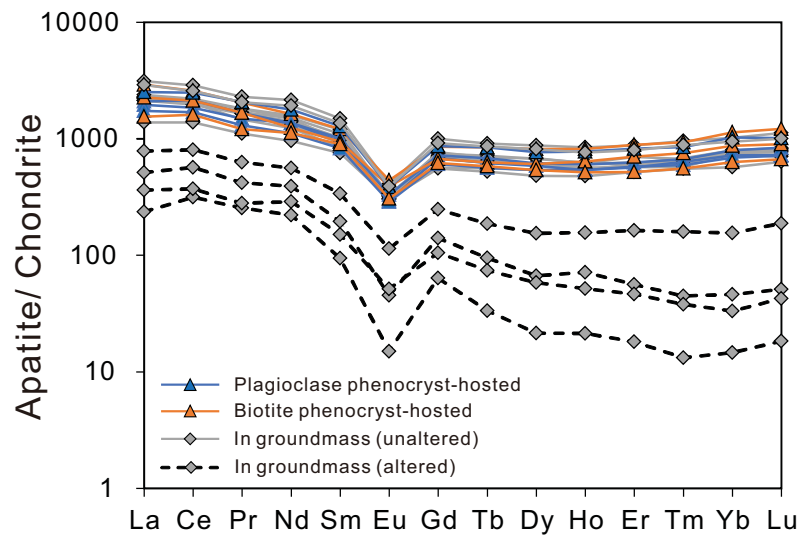


Figure 7

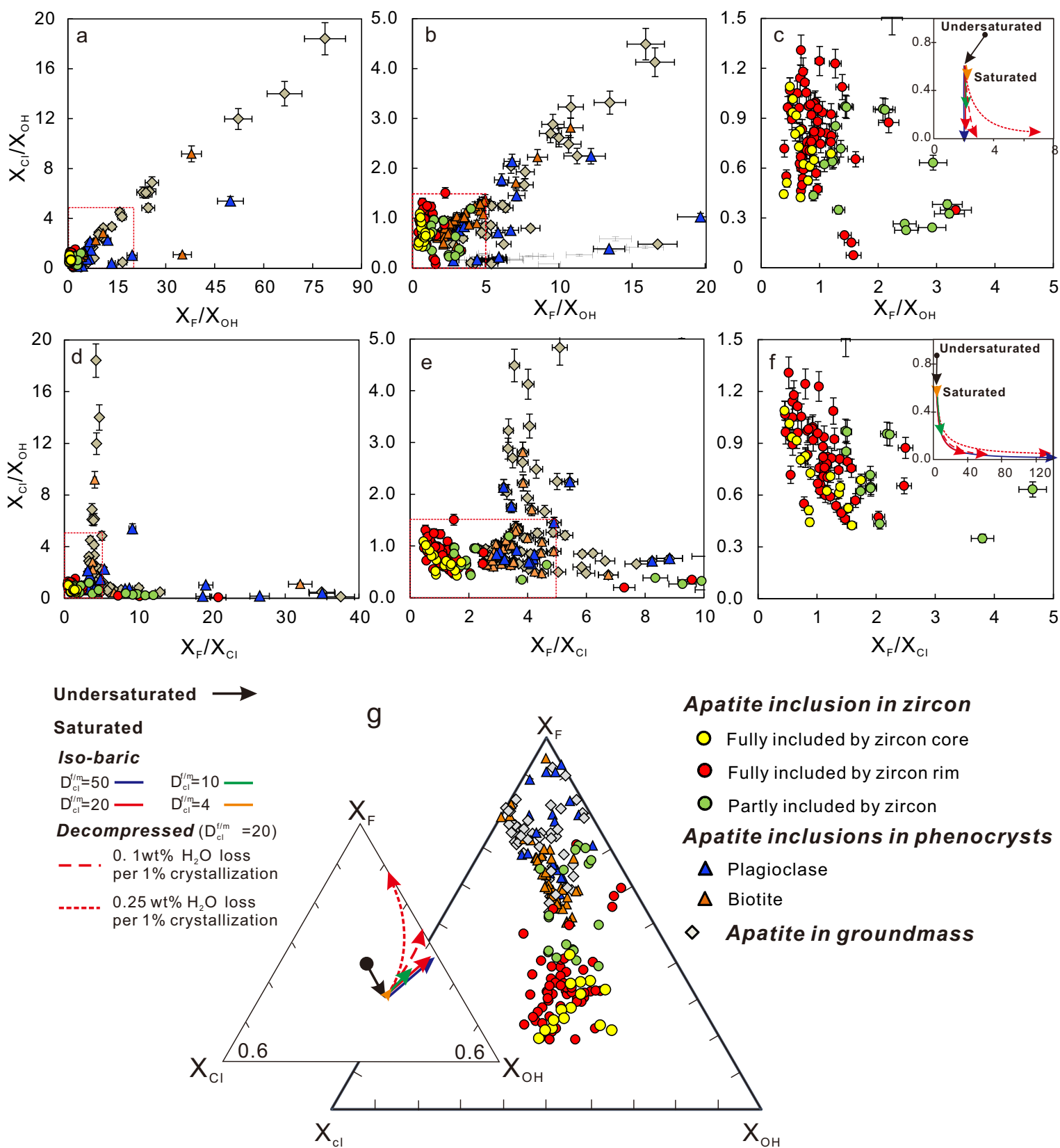


Figure 8

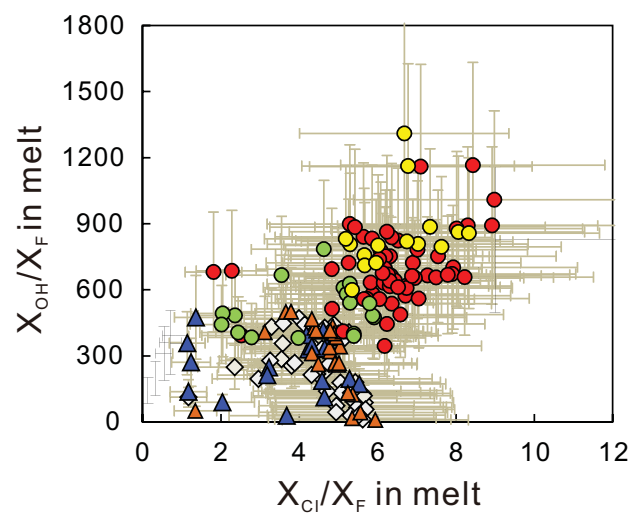


Figure 9

